Hydrodynamic Instabilities in High-Energy-Density Physics

by

Adrianna M. Angulo

A dissertation submitted in partial fulfillment
of the requirements for the degree of
Doctor of Philosophy
(Applied Physics)
in The University of Michigan
2023

Doctoral Committee:

Professor Carolyn C. Kuranz, Chair
Doctor Channing M. Huntington, Lawrence Livermore National Laboratory
Professor Eric Johnsen
Professor Yue Ying Lau
Professor Louise Willingale

Adrianna M. Angulo

aangulo@umich.edu

ORCID iD: 0000-0001-8701-2407

Reach for the Lasers. Safety Third.

)'(

ACKNOWLEDGEMENTS

I'd like to acknowledge my family- Mom, Pop, Michelle (and of course all the critters), for your unwavering support in me and my many interests. We are a gaggle of silly geese and boy do we let the world know it. I'm proud to come from a family that embraces the path less traveled and staying true to yourself. Dad, I'm truly sorry that I couldn't get you your sharks with lasers- maybe after my next degree.

Naturally, I must acknowledge my mentors. They say 'It takes a village to raise a child' but they should also say 'It takes a village to create a scientist.' Carolyn, RPD, Sabrina, Channing, Harry, Louisa, Louise, Liz, and Arturo have all shown me what it means to be an effective scientist by asking hard questions with a smile.

I am immeasurably thankful to my friends who have brought laughter into my life and brightness during dark times with blinky lights and music. I'm grateful for the friendships that transcended adolescence- Victoria, those that transcend academia- Mallory, Amina, Justin, Paul and Sarah, Sallee, and again Arturo, and those that transcend the dust- the Silverios, Craig, Sean, and The Neighbors.

Mario, who encompasses my life as family, mentorship, and friendship, deserves his own special acknowledgement category. Your smile, your child, and your hair adds a unique vibrancy to my life. I love you very much.

I'd also like to acknowledge Covid-19. Not positively, mind you, but as a reminder that you should always appreciate the present, even when it is uncomfortable. The global pandemic was terrible, but I am incredibly grateful for the friends and opportunities that arose from these 'unprecedented times.' For better and worse, the playa provides.

TABLE OF CONTENTS

LIST OF FIGURES

Figure

LIST OF TABLES

Table

ABSTRACT

The most proficient star-forming galaxies involve galactic filaments that supply gas to the center of the galactic halo. These galactic filaments are susceptible to the Kelvin-Helmholtz (KH) instability, which may potentially disrupt the filaments before they can penetrate deeply within the galaxy. In inertial confinement fusion, the Rayleigh Taylor (RT) instability is known to induce mixing or a turbulent transition, which in turn cools the hot spot and hinders ignition. The fine-scale features of the RT instability, which are difficult to image in HED systems, may help determine if the system is mixing or is transitioning to turbulence. Previous experiments conducted at the National Ignition Facility (NIF) utilized diagnostics with insufficient spatial and temporal resolution to diagnose the dynamics that occur along the RT structure. The Crystal Backlighter Imager (CBI) was developed to produce a high-resolution, x-ray radiograph capable of resolving the fine-scale features expected in these RT unstable systems. Although the resolution of the system has improved twofold, target constraints have prevented sufficient experimental resolution to be achieved.

This dissertation presents two HED experiments and observe two separate hydrodynamic instabilities. The first experiment presents how the experimental resolution of a system was improved by changing key parameters in the diagnostic and the target. A series of radiation hydrodynamic simulations were performed using the LLNL code, HYDRA to inform target and diagnostic designs for multiple shot days. By implementing interface spectral analysis and density variation analysis on the simulations and experimental data, I diagnose the perturbation growth to determine if the system meets the minimum requirement for the transition to turbulence. The second experiment describes a scaled, high-energy-density laboratory experiment on the Omega-EP laser that emulates and studies the cosmological process of filament supplying matter to the galactic halo. I use a radiography diagnostic to observe the KH instability on the filament boundary and tune hydrodynamic simulations performed using CRASH. From the data and tuned simulations, I determine the effects of the KH instability on filament and the conditions required for filament disruption.

CHAPTER I

Introduction

The story so far:
In the beginning the Universe was created.
This has made a lot of people very angry and been widely
regarded as a bad move.

–**Douglas Adams**

1.1 How it all started

In the dawn of space and time, mere seconds after its birth, the Universe was composed of fundamental particles, neutrinos, photons, and dark matter particles. This event is referred to as the Big Bang. During the early stages of the Universe, when it was small and hot but still rapidly expanding, ordinary matter (electrons, protons, and neutrons) was still coupled to photons. The radiation pressure from the coupled photons opposed matter accumulation due to gravitational effects. There would be no fluctuations in the distribution of ordinary matter to grow denser as long as matter remained coupled to photons. Meanwhile, dark matter particles had no such photon coupling. Fluctuations in the dark matter's distribution were allowed to grow and concentrations became denser. As the Universe continued to age and expand, dark matter particles created a network of dense, interconnected structures.

Once the Universe expanded enough to cool the ordinary matter, the ordinary matter decoupled from the photons. This had two prominent consequences. One is that protons and electrons combined and formed neutral hydrogen while enabling photons to propagate across the Universe (which we observe as the cosmic microwave background). This period is known as the Cosmic Dark Ages since there were no sources of light, only clouds of neutral hydrogen.

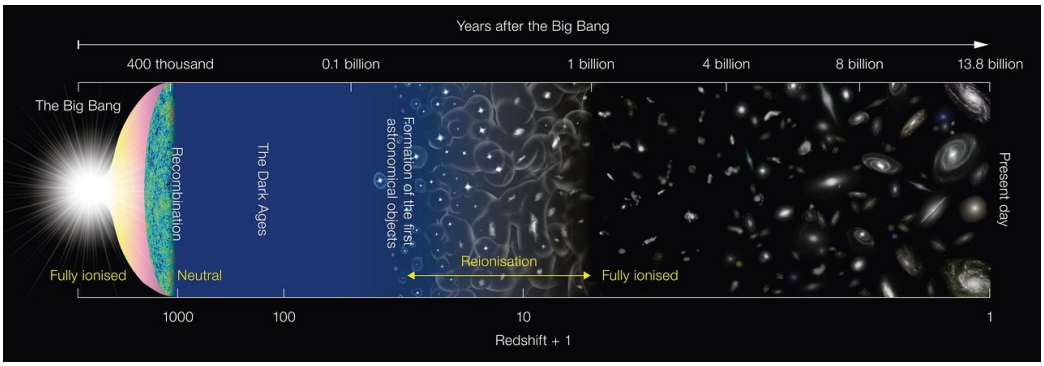

Figure 1.1: This schematic depicts the major milestones in the evolution of the Universe since the Big Bang. It is not to scale [1].

Second, ordinary matter began to assemble under gravitational effects. Ordinary matter could now feel the gravitation attractions from the already existing web of dark matter. Concentrations of dark and ordinary matter grew denser and more massive creating what we refer to as the cosmic web, a highly sub-structured network of knots and filaments of ordinary and dark matter. Eventually the densest concentrations gave rise to the first stars and first galaxies, whose emergence mark the end of the Dark Ages. Understanding these first sources is critical since they greatly influenced the formation of later objects such as galaxies.

Our understanding of the early Universe comes from a combination of visible light observation of the stars complemented by radiation measurements objects. The deeper we look into space the further back we see in time. Figure 1.1 shows the evolution of the Universe from the Big Bang to the current epoch. The region that is most relevant to this thesis is from about 13.5 to 13 billion years ago [1, 2].

1.2 Observational Astronomy

In 1990, the Hubble Space Telescope launched into orbit and revolutionized astronomy [3]. By operating in the ultraviolet to the near-infrared wavelength spectrum while located far above rain clouds and atmospheric distortions, it is designed to capture and focus light from distant objects in the Universe. The primary mirror of the Hubble Space Telescope is 2.4 meters (7.9 feet) in diameter and is made of ultra-low expansion glass. For over 30 years the Hubble has delivered stunning images

of stars, galaxies, supernova remnants and a glimpse of the physical processes that occur within these systems. Figure 1.2 shows the Hubble Deep Field, an image taken from the Hubble Space Telescope that gave astronomers the first clear look into early galaxy formation.

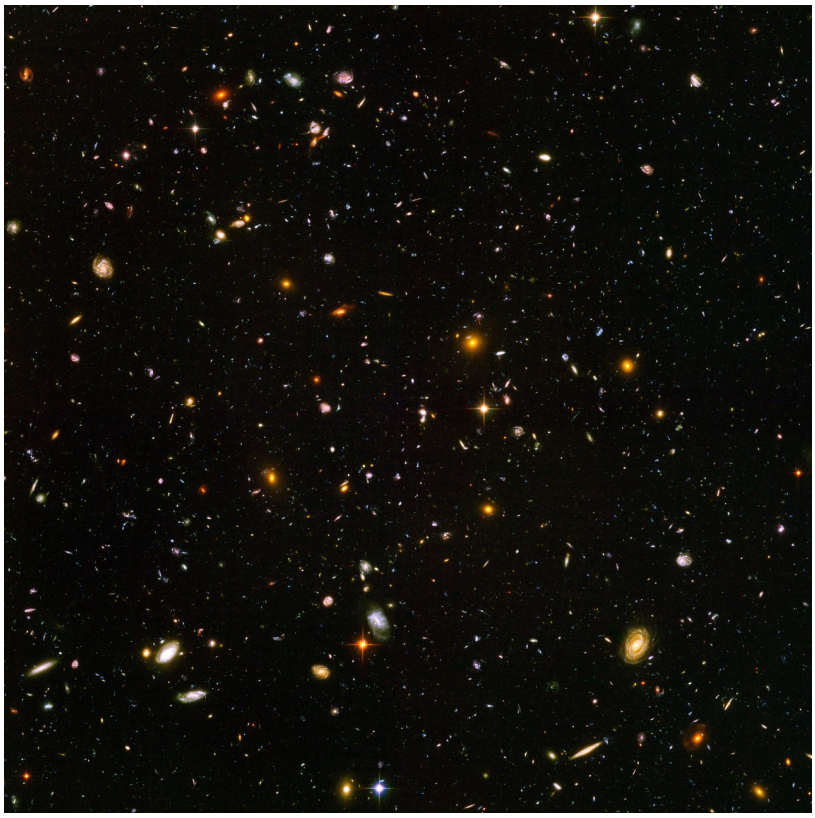

Figure 1.2: The Hubble Deep Field allowed astronomers to make many important discoveries about the Universe, most notably that the Universe is filled with a vast number of galaxies, each with its own unique properties and characteristics [3].

However, our Universe is continuously expanding. During the time it takes for light from an astronomical object to reach Earth, the Universe has grown in size, and the object's original location has gotten further away. Therefore, the wavelength of the light source becomes stretched, or redshifted. The further away the object is, the more its light's wavelength is red shifted. Astronomers denote the amount of redshift an object has undergone with the letter z. An object with a redshift of z emitted its light when the Universe was $1/(1+z)$ of its present size. So the higher the z, the further away the object is, the earlier it existed within our Universe. As mentioned before, the Hubble telescope's domain spanned to the near-infrared, therefore excluding high redshifted, or very early objects, from its detection. To cover this gap, a new optical

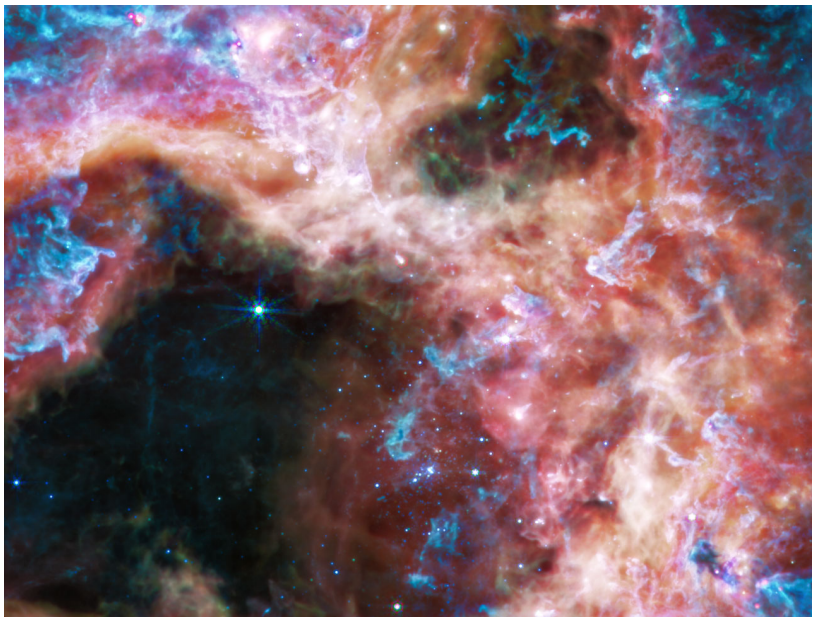

Figure 1.3: Newborn stars of the Tarantula nebula fade into the background while clouds of dust and gas take center stage, including hydrocarbons that will later form planets. Imaged with JWST's mid-infrared instrument [2].

telescope with high infrared resolution was recently put into commission.

The James Webb Space Telescope (occasionally referred to as JWST or simply just Webb) is a large infrared telescope [4]. It was successfully launched from the European Space Agency's spaceport in French Guiana on December 25, 2021. JWST operates in a halo which circles around a point in space referred to as the Sun-Earth L_2 Lagrange point. This point lies about 930,000 miles beyond Earth's orbit around the sun. It can orbit the Sun in synchrony with the Earth which protects the telescope. The telescope is equipped with a primary mirror that is made up of 18 hexagonal segments and measures 6.5 meters (21 feet) in diameter. The mirror is coated with a thin layer of gold to help it reflect infrared light more efficiently. The telescope also has a number of science instruments that are designed to detect and analyze different types of light, including visible light, near-infrared light, and mid-infrared light. Figure 1.3 shows a recent infrared- image of the Tarantula nebula captured by the JWST [2].

Observational astronomy plays a critical role in helping astronomers and scientists to understand the Universe. It uses telescopes and other instruments to allow us to observe and collect data about distant objects. However, laboratory astrophysics

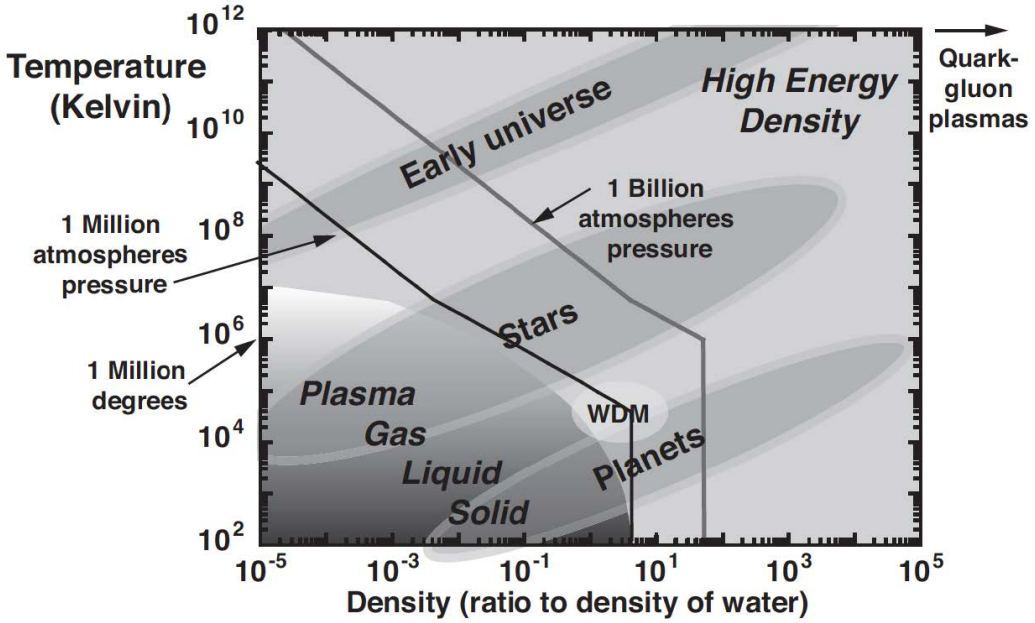

Figure 1.4: From *High-Energy Density Physics: Foundations of Inertial Fusion and Experimental Astrophysics* [5]. Astrophysical phenomenon lie within HED regimes as a function of density and temperature.

is able to combine the principles of observable astronomy and laboratory physics to study processes that occur in the Universe on Earth. Laboratory astrophysics can be used to test theoretical models and predictions about the behavior of matter and energy in the Universe, and it can also provide insights into the properties and behaviors of objects in the Universe that are difficult or impossible to observe directly.

1.3 High-Energy-Density Laboratory Astrophysics

Everything observed by telescopes of the distant Universe consists of a plasma. A subset of environments that exist within this plasma consist of High-Energy-Density (HED) systems. Generally put, HED systems are systems whose energy density (i.e. pressure) is greater than 1 Mbar (or 10^5 J/cm^3 or 10^{11} Pa) [5]. These systems are typically found in extreme environments, such as the cores of stars and the interiors of planets. Figure 1.4 shows where HED and astrophysical systems are in density-temperature space [5].

HED physics has a long history, with some of the earliest work in the field dating back to the early 20th century [6]. In the 1930s and 1940s, researchers began studying plasma in the laboratory, using electric discharge tubes to create plasma

and investigate its properties. In the 1950s and 1960s, research in HED physics was driven largely by the development of nuclear weapons and the need to understand the behavior of nuclear materials under extreme conditions [7].

In the 1970s and 1980s, research in HED physics was driven by the development of fusion as a potential energy source. Fusion is the process by which two atomic nuclei combine to form a heavier nucleus, releasing a large amount of energy in the process. Researchers sought to understand the conditions under which fusion could be sustained and controlled in the laboratory [8, 9]. New technologies further expanded the scope of HED physics in the 1990s and 2000s. Laser-driven shock compression and high-power lasers allowed researchers to create and study extreme conditions in the laboratory. Today, HED physics research continues to be driven by a variety of applications, including the development of fusion energy, the study of planetary interiors, and the investigation of fundamental physical phenomena under extreme conditions.

1.4 How laboratory experiments can inform our understanding of astrophysical systems

Astrophysically relevant length scales occur on the order of light-years throughout years, or even millions of years. Meanwhile, terrestrial fluid dynamics typically exist between nanometer and meter length scales for a duration of nanoseconds to hours. Laboratory astrophysics experiments can meaningfully contribute to the understanding of astrophysical systems by emulating the astrophysical time and length scales.. To do so, both systems must be described by the same relevant equations. For example, for hydrodynamic systems, such as the ones described in this dissertation, Euler's equations describe both the astrophysical system and the 'scaled' HED experiment. We can then determine how well the laboratory system is scaled to the astrophysical system by implementing Ryutov's scaling [10].

In his paper, Ryutov determined a dimensionless parameter that remains unchanged between an astrophysical and laboratory system. For a hydrodynamic system, we can employ Euler's equations (further discussed in Chapter II). The variables L^*, ρ^*, p^*, u^* denote characteristic the spatial, density, pressure, and velocity scales of the problem. From the characteristic variables, dimensionless variables $\tilde{L}$, $\tilde{t}$, $\tilde{\rho}$, $\tilde{p}$, $\tilde{u}$ are introduced as:

$$\tilde{L} = \frac{L}{L^*}, \qquad \tilde{t} = \frac{t}{L^*}\sqrt{\frac{p^*}{\rho^*}}, \qquad \tilde{\rho} = \frac{\rho}{\rho^*}, \qquad \tilde{p} = \frac{p}{p^*}, \tag{1.1}$$

and

$$\tilde{\boldsymbol{u}} = \boldsymbol{u}\sqrt{\frac{\rho^*}{p^*}}. \tag{1.2}$$

The parameter,

$$\mathrm{Ry} = \mathrm{u}^*\sqrt{\frac{\rho^*}{\mathrm{p}^*}}, \tag{1.3}$$

is the Ryutov number. When the Ryutov number is invariant between the two systems and the initial states are geometrically similar, the two hydrodynamic systems have the same dimensionless equations and the same dimensionless characteristic conditions. This implies that the systems will evolve similarly in a scaled sense [10, 11]. We can establish that a pair of systems has Ryutov scaling in a relatively direct and straightforward manner by choosing the appropriate characteristic scales. The phrase 'a well-scaled experiment' indicates that the Ryutov number of the laboratory experiment and the astrophysical system are roughly equivalent [10].

1.5 Laser-driven, shock-tube experiments

A 'typical' HED target (see Figure 1.5) consists of three basic components: the laser, the driver, and the physics package. First, a set of laser beams are focused onto the driver. The laser wavelengths typically range from 351 nm to 1052 nm for a pulse duration of 0.1-10 ns, with individual beam energies of order $\sim$ kJ [7, 12].

The gold component in Figure 1.5 describes the 'driver'. The driver, or drive package, refers to the surface that is irradiated by the laser or laser-generated x-rays. For a 'direct drive' experiment, the beams are focused directly onto the driver with a relatively uniform, $\sim$ 1 mm diameter focal spot producing irradiances on the order of $\sim 10^{14}$ W/cm^2 [11]. For an 'indirect drive' experiment, the driver is attached to a gold can called a hohlraum (the German word for 'a hollow place') or halfraum. In this scenario, the laser beams are focused to the inner walls of the hohlraum. The resultant plasma then produces an x-ray flux that is incident into the physics package [9]. Both indirect and direct drives create an ablation plume that acts as a rocket and induces a shock, or pressure source, for the physics package [13]. While the physics package has many variations depending on the experimental goal, the physics

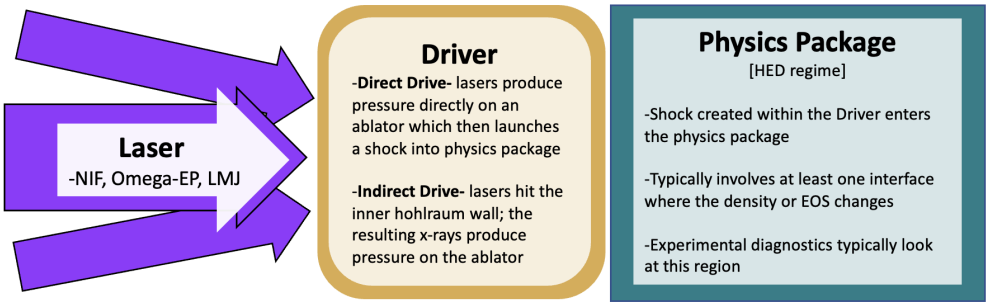

Figure 1.5: A 'standard' shock-driven, HED target is simplified into three components: the laser, the driver, and the physics package. The laser deposits energy onto the driver, which in turn produces a shock into the physics package [5].

packages described in this dissertation are designed to produce systems susceptible to the Rayleigh-Taylor instability or the Kelvin-Helmholtz instability. These instabilities are further described in Chapters II, IV, and V.

1.6 Facilities

The OMEGA Extended-Performance (OMEGA EP) laser is a high-energy, long and short-pulse laser system located at the University of Rochester's Laboratory for Laser Energetics (LLE). It has been in operation since 2008 as addition to the 60-beam UV OMEGA Laser System and extends the performance (hence the name 'Extended Performance') and capabilities of the Omega Laser Facility at LLE. OMEGA EP has four, frequency-tripled, kJ-class, independently-configurable NIF-scale beamlines, two of which can be compressed into short, petawatt-class pulses.

The National Ignition Facility (NIF) is a large-scale laser facility located at the Lawrence Livermore National Laboratory in Livermore, California. The NIF consists of a complex system of lasers, optics, and diagnostic instruments that are used to deliver 192 beams to a small target to create HED conditions. A NIF quad consists of a group of 4 beams and are grouped in inner and outer cones distinguished by polar angles. The NIF is used for a wide range of scientific and technological research, including the study of HED physics, the development of advanced materials, and the investigation of the properties of matter under extreme conditions. It is also used for the testing and validation of weapons simulations and for the study of the fundamental physics of laser-plasma interactions.

1.7 Thesis Organization

In Chapter II, I discuss the governing equations of fluid dynamics typically used to describe certain HED systems. I introduce single-mode linear stability theory for the Rayleigh-Taylor and Kelvin-Helmholtz instabilities. Finally, I discuss the definitions of turbulence and the criteria to diagnose its onset.

In Chapter III, I introduce a common method to observe hydrodynamic instabilities in HED experiments with x-ray diagnostics. I describe the mechanics behind the Crystal Backlighter Imager and Spherical Crystal Imager, both spherically bent crystals located at the National Ignition Facility and Laser for Laboratory Energetics respectively.

In Chapter IV, I describe a campaign conducted on the National Ignition Facility. The campaign sought to improve the experimental resolution of a well fielded target system by changing key parameters in the x-ray diagnostic and the target. I describe a series of radiation hydrodynamic simulations I performed using the LLNL code, HYDRA to inform target and diagnostic designs for multiple shot days. I then show the resulting experimental radiographs taken on the NIF that resolve the fine-scale features expected in these RT unstable systems with unprecedented clarity. By implementing interface spectral analysis and density variation analysis on the simulations and experimental data, I am able to diagnose perturbation growth to determine if the system meets the minimum requirement for the transition to turbulence. The improved resolution of the system will allow new observations to study the RT instability's involvement in mixing and the transition to turbulence in the HED regime.

In Chapter V, I illustrate that most proficient star forming galaxies, starburst galaxies, are those that involve filaments that withstand the shock that forms at the edge of the galactic halo and transport matter deep into the galactic disc. The cold, dense matter within the filament moves within the hot gaseous background, indicating that the filament boundary is likely Kelvin-Helmholtz (KH) unstable. I describe a scaled, HED laboratory experiment conducted on the Omega EP laser that emulates and studies the cosmological process of a cold stream penetrating a shocked region. Using a radiography diagnostic, we observe the KH instability on the filament boundary and compare the results to hydrodynamic simulations performed using CRASH, a radiation hydrodynamics code developed at the University of Michigan.

From the data and simulations, I examine the extent to which the KH instability can inhibit mass delivery to the galactic disc.

1.8 Contributions

While in the Applied Physics Department at the University of Michigan, I have worked on many projects, some not discussed in this thesis, that have provided experience in a variety of research areas in HED science. To me, it was important that I develop a varied set of skills during graduate school; as such I have dedicated equal parts of my time to research as an experimentalist and as a designer.

As an experimentalist, I led several scaled laboratory astrophysics campaigns as Principal Investigator on the OMEGA EP laser at the Laboratory for Laser Energetics. One of these experiments, described in this thesis, studied the Kelvin-Helmholtz instability of an astrophysical system. Graduate student Shane Coffing performed the hydrodynamic simulations that informed this experiment, while I executed the experiment.

During my graduate student residency at Lawrence Livermore National Laboratory, I acted as designer for the High Resolution Turbulence (HRT) Campaign by performing simulations using HYDRA to inform target designs and diagnostic optimization for 8 shot days conducted on the NIF. My simulations and designs were presented to the HED council and contributed to the NIF experimental time awarded to the HRT campaign. I present analyzed data and simulations from three of those shot days in this dissertation.

Much of the work I have done was in collaboration with scientists at the Laboratory for Laser Energetics, Lawrence Livermore National Laboratory, and Los Alamos National Laboratory and has resulted in original research, invited talks, and subsequent publications as a first and second author.

CHAPTER II

Hydrodynamic Instabilities

2.1 The Fluid Approximation

This chapter discusses the governing equations of fluid dynamics that we use to describe certain HED systems. Then I introduce single-mode linear stability theory for the RT instability, its venture into nonlinearity, and finally the effects of vorticity along the instability.

A plasma, the 4th state of matter, is a gas that has been heated or compressed such that the bound electrons are stripped from their nuclei. This results in a system with separate populations of ions and electrons. Under some conditions one can use kinetic theory to describe the single-particle motion of the ions and electrons, it is oftentimes computationally expensive. Instead, it is possible to use a fluid model to approximate certain phenomena with reasonable accuracy.

To treat the plasma as a fluid, we subdivide into a large number of small, moving fluid elements that each contain a large number of particles. These fluid elements contain a large number of particles and have a high enough collisionality that the particles are confined to a region size comparable to the mean free path. The mean free path, $\lambda = 1/n\sigma$, is the average distance an incident particle travels before it has a collision and is the inverse of the number density, n, and the cross section, σ. In other words, a high number density along with a large cross section yields a shorter distance particle travels before undergoing a collision. An importance consequence is that the chosen fluid element and other length scales of interest, L, must be larger than the mean free path for the fluid approximation to hold, $L \gg \lambda$.

Another simplifying aspect of the fluid element is that each fluid element is can be described by the average macroscopic properties of the particles centered at point $\mathbf{r}$ at time t. Plasma properties such as the density $n_{\text{electron}}(\mathbf{r}, t)$ and $n_{\text{ion}}(\mathbf{r}, t)$, macroscopic flow velocities $\boldsymbol{u}_{\mathbf{electron}}(\boldsymbol{r}, t)$ and $\boldsymbol{u}_{\mathbf{ion}}(\boldsymbol{r}, t)$, pressures $p_{\text{electron}}(\boldsymbol{r}, t)$ and $p_{\text{ion}}(\boldsymbol{r}, t)$, and temperature $T_{\text{electron}}(\boldsymbol{r}, t)$ and $T_{\text{ion}}(\boldsymbol{r}, t)$ can be found using the fluid description [14].

Finally, Euler's equations conservation of mass, momentum, and energy, can be used to describe the evolution of the plasma fluid. Euler's equations of conservation of mass, momentum, and energy are shown below:

$$\frac{\partial \rho}{\partial t} + \nabla \cdot \rho \boldsymbol{u} = 0, \tag{2.1}$$

$$\rho \left(\frac{\partial u}{\partial t} + \boldsymbol{u} \cdot \nabla u \right) = -\nabla p, \tag{2.2}$$

$$\frac{\partial \rho}{\partial t} + \boldsymbol{u} \cdot \nabla p = -\gamma p \nabla \cdot \boldsymbol{u}. \tag{2.3}$$

In these equations, ρ is the mass density, u is the velocity, p is the pressure, and γ is the adiabatic index. The three equations are then used to determine how the plasma and potential instabilities behave.

Since we can describe some plasmas as a fluid, it also means that it it can be subjected to hydrodynamic instabilities. Hydrodynamic instabilities result in fluid mixing and affect overall flow dynamics. These instabilities rely on the existence of a free energy source that can drive growth of any perturbations at an interface beyond restoring forces. The sources of this energy is different for each of the three common instabilities. For the Rayleigh-Taylor (RT) instability, a gravitational force or surface acceleration that drives a dense material into a lighter material thereby displacing the lighter material that is unable to support it [15, 16]. The Richtmyer-Meshkov (RM) instability arises due to the impulsive acceleration of an interface [17]. Finally the source of Kelvin-Helmholtz (KH) instability is the shearing that occurs between the surface [18]. The remainder of this Chapter is dedicated to discussing the KH instability and the RT instability.

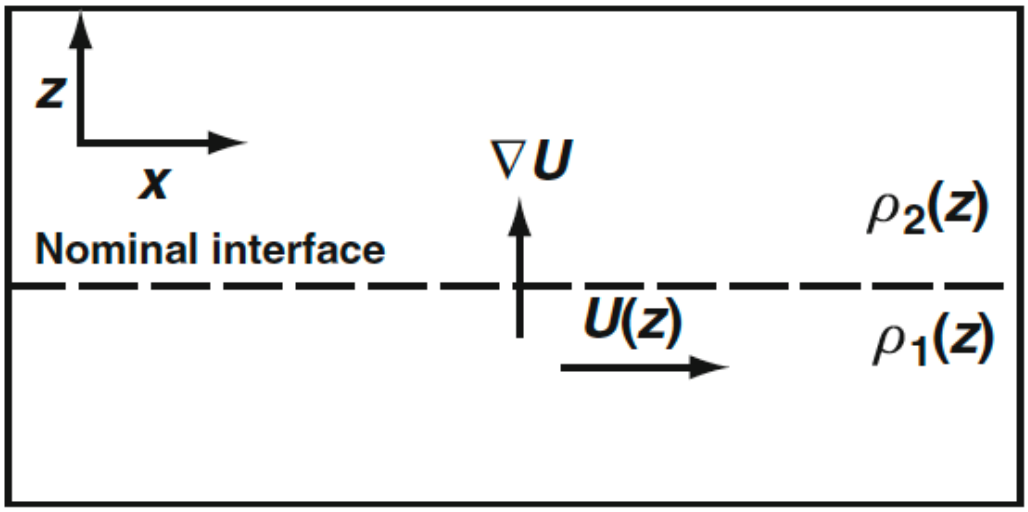

Figure 2.1: The Kelvin-Helmholtz instability geometric layout. The velocity and density gradient is in the z-direction, across the nominal interface. Reproduced from [11].

2.2 The Kelvin-Helmholtz Instability

The Kelvin-Helmholtz instability (KH) develops when there is a shear flow present in the system. A shear flow consists of two parallel fluids flowing past one another with a velocity difference and exists within the shear layer. The shear layer is the transition region where significant velocity gradient exists parallel to the flow. The velocity shear between the two fluids causes the perturbations on the interface to grow. As the perturbation amplitude continues to grow, it eventually saturates into characteristic vortical structures. These structures, also known as "rollups", are responsible for intermixing the two regions. The KH instability leads to momentum and heat transport while mixing the two fluid streams.

To determine the KH instability growth rate, we simplify the unstable system by assuming there is a zero-thickness interface between the two fluids in the x-y plane. The initial flow, U, is parallel to the x-axis, and the ∇U and $\nabla\rho$ are parallel to the z-axis while $\delta\rho$ and δp are the first order density and pressure perturbations. The transition region where the velocity changes quickly but remains along the same axis is referred to as the shear layer. Figure 2.1 shows the direction of the velocity and density gradients in a KH unstable system.

Given this configuration, we start with the linearized continuity and momentum equations of a perturbed system:

$$\frac{\partial \delta\rho}{\partial t} + \mathbf{U}\cdot\nabla\delta\rho + \mathbf{u}\cdot\nabla\rho = 0, \tag{2.4}$$

$$\rho\frac{\delta \mathbf{u}}{\delta t} + \rho\mathbf{U}\cdot\nabla u + \rho\mathbf{u}\cdot\nabla U = -\nabla\delta p - g\delta\rho\hat{z}. \tag{2.5}$$

We then incorporate the requirement for continuity of the surface,

$$\frac{\partial \delta\mathbf{x_s}}{\partial t} + \mathbf{U}\cdot\nabla\delta x_s = \mathbf{u_s}, \tag{2.6}$$

where δx_s is the location of a point on the interface after it has moved and $\mathbf{u_s}$ is the velocity of that point.

To solve for the unstable behavior, we break up continuity and momentum equations into their three directions with $\mathbf{u}$ = (u,v,w):

$$\rho\frac{\partial u}{\partial t} + \rho U\frac{\partial}{\partial x}u + \rho w\frac{\partial}{\partial z}U = -\frac{\partial}{\partial x}\delta p, \tag{2.7}$$

$$\rho\frac{\partial v}{\partial t} + \rho U\frac{\partial}{\partial x}v = -\frac{\partial}{\partial y}\delta p, \tag{2.8}$$

$$\rho\frac{\partial w}{\partial t} + \rho U\frac{\partial}{\partial x}w = -\frac{\partial}{\partial z}\delta p - g\delta\rho. \tag{2.9}$$

We assume surface waves in the x-y plane grow exponentially in time and also have an oscillatory component, so we can assume the linearized amplitudes will be proportional to $\exp[i(k_x x + k_y y + nt)]$. Note that the instability grows with a negative imaginary n. Since U varies with z and by eliminating δp, a single differential equation for w is found,

$$-k^2\rho(n+k_xU)w + \frac{\partial}{\partial z}\left[\rho(n+k_xU)\frac{\partial w}{\partial z}\right] - \frac{\partial}{\partial z}\left(\rho k_x w\frac{\partial U}{\partial z}\right) = g\frac{wk^2}{(n+k_xU)}\frac{\partial\rho}{\partial z}. \tag{2.10}$$

Equation 2.10 can be further simplified by separating the role of density from the equation whose density profiles is large compared to the perturbation wavelength. If the boundary is continuous at the interface, we have

$$\frac{w_2}{(n+k_xU_2)} = \frac{w_1}{(n+k_xU_1)}, \tag{2.11}$$

with the subscripts 1 and 2 referring to either side of the boundaries. To then find the boundary condition across the KH interface we use

$$\begin{aligned} gk^2\left(\frac{w}{n+k_xU}\right)^2(\rho_2-\rho_1) = \\ \rho_2(n+k_xU_2)\frac{\partial w_2}{\partial z} - \rho_1(n+k_xU_1)\frac{\partial w_1}{\partial z} + k_x\left(-\rho_2 w_2\frac{\partial U_2}{z} + \rho_1 w_1\frac{\partial U_1}{\partial z}\right). \end{aligned} \tag{2.12}$$

Now that the boundary condition at the interface is known, we can determine how it evolves over time. To get the general features, we consider a simple case of two fluids with uniform densities and uniform velocities that change only at the interface. Equation 2.10 is then reduced to

$$-k^2w + \frac{\partial^2 w}{\partial z^2} = 0. \tag{2.13}$$

The solutions of this differential equation are a linear combination of the following terms:

$$w_+ = A_2e^{-kz}, \tag{2.14}$$

$$w_- = A_1e^{kz}. \tag{2.15}$$

where w_+ occurs above the interface, w_- occurs below the interface, and coefficients A_1 and A_2 satisfy the boundary condition. To further simplify the equations, we work in the frame of reference of the average velocity of the two regions, so that $U_2 = \Delta U/2$ $U_1 = -\Delta U/2$.

Then at the interface and applying surface continuity at the boundary conditions, we get

$$\frac{A_2}{n+k_xU_2}e^{-kz}\bigg|_{-z} = \frac{A_1}{n+k_xU_1}e^{kz}\bigg|_{z}. \tag{2.16}$$

From Equation 2.11, we can solve for the constant A_2 as

$$A_2 = A_1 \frac{n + k_x U_2}{n + k_x U_1}. \tag{2.17}$$

Finally, we are left with the algebraic expression

$$0 = \rho_2 (n + k_x U_2)^2 + \rho_1 (n + k_x U_1)^2, \tag{2.18}$$

whose solution is the instability growth rate,

$$n = -k_x \frac{A_n}{2} \pm i k_x \Delta U \frac{\sqrt{\rho_1 \rho_2}}{(\rho_1 + \rho_2)}. \tag{2.19}$$

The real part of n describes the wave propagation along the surface of the chosen frame of reference. The negative imaginary part is the exponential growth rate.

$$\gamma_{\text{ic}} = \frac{k \Delta U}{2} \frac{\sqrt{\rho_1 \rho 2}}{\rho_1 + \rho_2} = \frac{k \Delta u}{2} \sqrt{1 - A}. \tag{2.20}$$

Equation 2.20 describes the perturbation growth rate on the interface with a small amplitude to wavelength ratio. There are a few implications from Equation 2.20. The first implication is that there is no perturbation growth without a velocity difference. Next, instability growth is proportional to the parallel component of the wavenumber and that smaller wavelengths perturbations grow more rapidly. Finally, when $\rho_1 = \rho 2$, $\gamma_{\text{ic}} = k_x \Delta U / 2$.

Earlier we have assumed the fluid is incompressible. Incompressible KH instability occurs when the fluids involved are assumed to be incompressible, meaning their density does not change as a result of the pressure changes in the fluid (i.e. $\nabla \cdot \mathbf{u} = 0$). On the other hand, when the fluids involved are compressible, their density can change as a result of the pressure changes in the fluid. In this case, the instability is characterized by the Mach number of the fluid. Sound waves can interact with the fluid interface and affect the incompressible growth rate. The growth rate of the compressible KH instability is

$$\gamma_{\text{c}} = \left[\frac{k \Delta u}{2} \sqrt{1 - A^2} \right] \frac{\sqrt{-1 - M_C^2 + \sqrt{1 + 4 M_C^2}}}{M_C}, \tag{2.21}$$

where M_C is the convective Mach number, $M_C = \Delta u / (c_1 + c_2)$, and c_1 and c_2 are the sound speeds of the two materials. In the limit where $M_C \to 0$, the incompressible growth rate is restored $\gamma_{\text{c}} = \gamma_{\text{ic}}$.

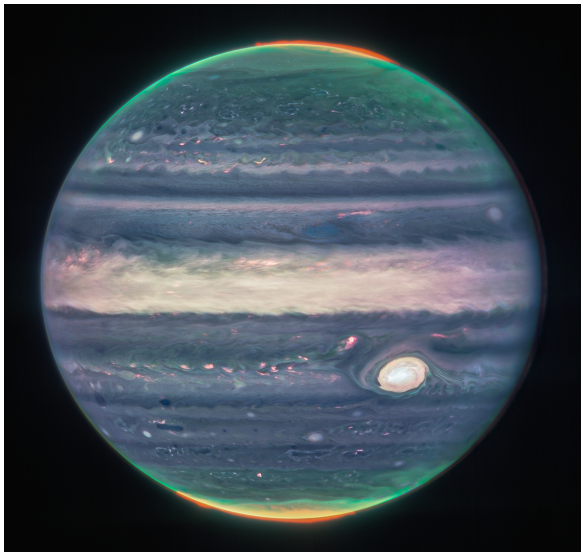

Figure 2.2: Webb NIRCam composite image of Jupiter from three filters. Jupiter's clouds are a famous example of the Kelvin-Helmholtz instability. Credit: NASA, ESA, CSA, Jupiter ERS Team; image processing by Judy Schmidt.

The KH instability is readily observable not only in water and Earth and Jupiter's clouds (see Figure 2.2), but also plays a significant role in non-linear RT evolution causing the characteristic mushroom shape on the RT spike tip.

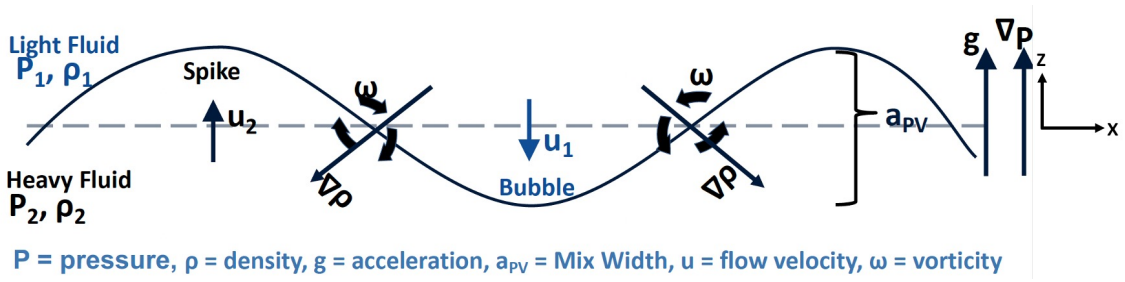

Figure 2.3: Diagram of the Rayleigh-Taylor Instability. Fingers of dense materials, 'spikes' interpenetrate less dense fluid, 'bubbles', when the heavy fluid is accelerated against the lighter fluid. Adapted from [19].

2.3 The Rayleigh-Taylor Instability

The classical Rayleigh-Taylor (RT) instability scenario that we see everyday consists of two incompressible and viscid fluids of differing densities in a gravitational field. Figure 2.3 shows a simplifed schematic of an RT unstable system. If the less dense, or 'lighter' fluid has a higher gravitational potential than the denser, or 'heavier' fluid, then the system is said to be RT stable. But, if we 'flip the script' so that the heavier fluid is now at a higher gravitational potential and supported by the lighter fluid, our system is now RT unstable. The classical question then becomes – how do small perturbations on the fluid interface behave once it is disturbed from its static initial condition?

To understand how a perturbation subjected to the RT instability grows, we can derive the growth rate of the perturbations on the fluid boundary. Therefore, any perturbation on the boundary can be represented with a sum of Fourier modes, $e^{i(k_x x + k_y y)}$, where k is the total wavenumber, $k = \sqrt{k_x^2 + k_y^2} = 2\pi/\lambda$. However, to simplify the problem we can consider a single-mode RT unstable system and determine the RT linear growth rate.

To solve the RT linear growth rate for a single-mode system, we describe the initial interface perturbation at the fluid boundary with a single sine function of a known amplitude, a and wavelength, λ. First equations for conservation of mass and momentum are expanded and linearized by considering small deviations in ρ , p, and $\mathbf{u}$. We then solve for the growth of the perturbations to determine if the system is stable or unstable. Once again we start with Euler's continuity and momentum equations:

$$\frac{\partial \rho}{\partial t} + \mathbf{u} \cdot \nabla \rho = 0, \tag{2.22}$$

$$\rho \frac{\partial \mathbf{u}}{\partial t} + \rho \mathbf{u} \cdot \nabla \mathbf{u} = -\nabla p + \rho \mathbf{g}, \tag{2.23}$$

where $\mathbf{g}$ is the effective acceleration in $\hat{\mathbf{z}}$. To expand about the slightly perturbed state, we take the rest values of p, ρ, and u to $p = p_0 + \delta p$, $\rho = \rho_0 + \delta \rho$, $u = \delta u$ where δ denotes a small value multiple. Note: $u_0 = 0$ since the system is initially at rest.

To linearize these values, the perturbed quantities are substituted into Equation 2.22 and Equation 2.23

$$\frac{\partial}{\partial t}(\rho_0 + \rho_1) + \mathbf{u} \cdot \nabla \rho_0 + \rho_1 = 0, \tag{2.24}$$

$$\frac{\partial \rho_1}{\partial t} + \mathbf{u} \cdot \nabla \rho = 0, \tag{2.25}$$

and

$$(\rho_0 + \rho_1)\frac{\partial \mathbf{u}}{\partial t} + (\rho_0 + \rho_1)\mathbf{u} \cdot \nabla u = -\nabla(p_0 + p_1) + \rho \mathbf{g}, \tag{2.26}$$

$$\rho_0 \frac{\partial \mathbf{u}}{\partial t} = -\nabla p_0 + \rho_1 \mathbf{g}. \tag{2.27}$$

The resulting 1st order equations are then written as

$$\frac{\partial \rho_1}{\partial t} + \nabla \cdot (\rho_0 \mathbf{u_1} + \rho_1 \mathbf{u_0}) = 0, \tag{2.28}$$

and

$$\rho_0 \frac{\partial \mathbf{u_1}}{\partial t} = -\nabla p_0 + \rho_1 \mathbf{g}. \tag{2.29}$$

Finally, we find growth of the amplitude, a, of a small single-mode perturbation is given by

$$\frac{d^2 a}{dt^2} = gkA, \tag{2.30}$$

where k = $2\pi/\lambda$ is the wavenumber, and A is the Atwood number

$$A = \frac{\rho_2 - \rho_1}{\rho_2 + \rho_1}, \tag{2.31}$$

and the growth rate, γ, is given by

$$\gamma = \pm(gkA)^{1/2}. \tag{2.32}$$

As the amplitude continues to grow, the linear phase of the RT instability eventually transitions to the nonlinear regime.

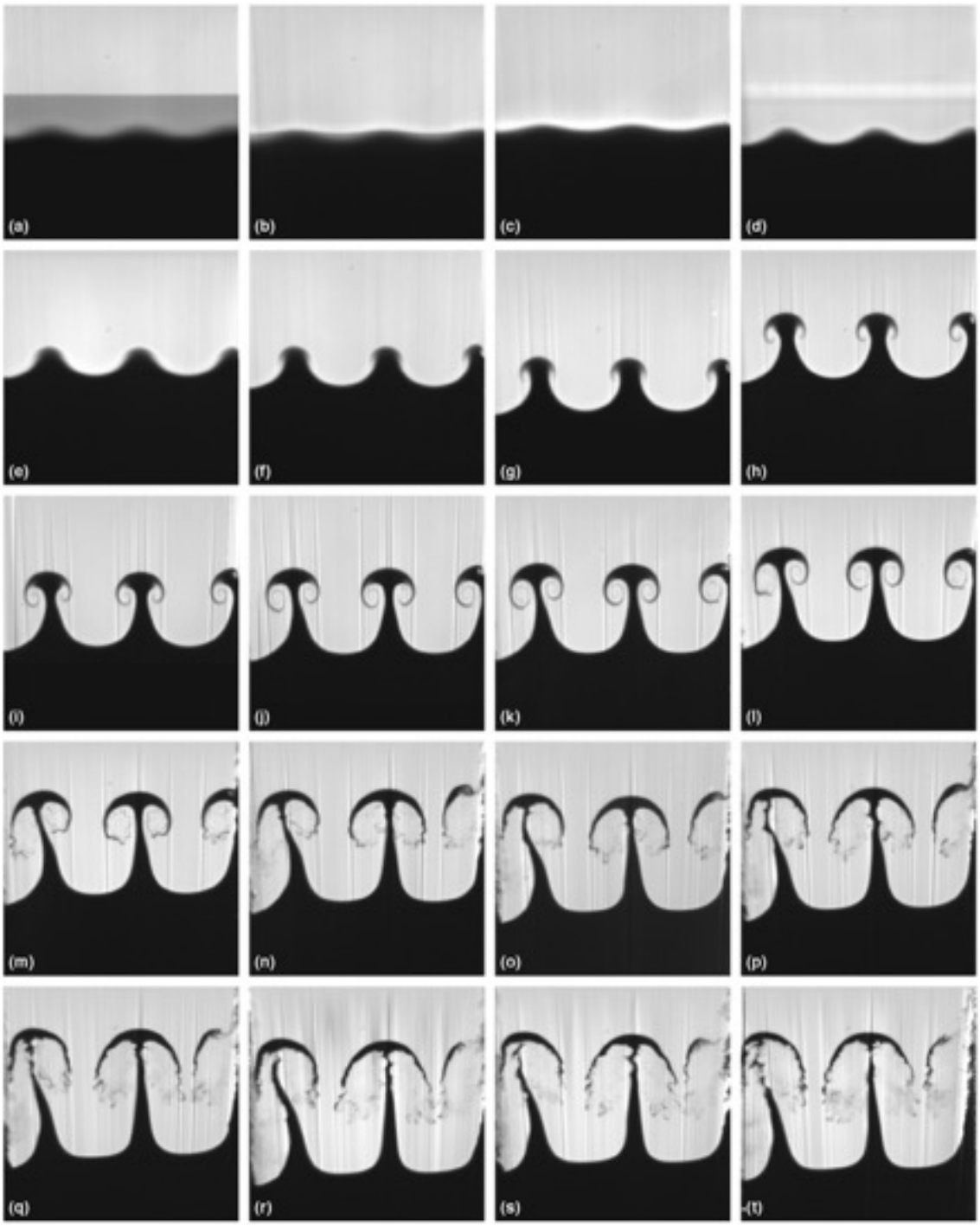

Figure 2.4: Images from 20 classical fluids experiments assembled to form a time sequence for the RT instability evolution. Adapted from reference [20].

As hydrodynamic instabilities further evolve, and the amplitude grows to approximately 10% of the wavelength, the system approaches the early nonlinear stage [18, 21]. It is during this stage that nonlinear terms become large enough to make significant contributions to the interface features that affect the growth rate [18, 22]. Vorticity, the curl of the velocity, is eventually introduced when the density gradient becomes misaligned from the pressure gradient along the length of the spike. It creates vortex features that cause the spike to broaden as it grows. It is also possible that the vorticity induces a transition to turbulence within this vortex feature. However, this is not a guaranteed result [20].

2.4 Vorticity

When a shock wave interacts with the material interface at a non-normal angle, vorticity is deposited on the interface. Vorticity can be understood through the vorticity transport equation,

$$\frac{\partial \omega}{\partial t} + \boldsymbol{\nabla} \times (\omega \times \mathbf{u}) = \frac{1}{\rho^2} \boldsymbol{\nabla}\rho \times \boldsymbol{\nabla} p, \tag{2.33}$$

where $\mathbf{u} \equiv (u, v, w)$ is the velocity vector and $\omega \equiv \boldsymbol{\nabla} \times \mathbf{u}$ is the vorticity . The term on the right hand side, the baroclinic production term, is what leads to vorticity when $|\boldsymbol{\nabla} p \times \boldsymbol{\nabla}\rho| > 0$.

Since the shock wave interacts with the interface for a short time compared to the instability growth time, 2.33 is reduced to

$$\frac{\partial \omega}{\partial t} \approx \frac{1}{\rho^2} \boldsymbol{\nabla}\rho \times \boldsymbol{\nabla} p. \tag{2.34}$$

The pressure gradient in Equation 2.34, $\boldsymbol{\nabla} p$ is determined by the momentum equation,

$$\frac{\partial \rho \mathbf{u}}{\partial t} + \boldsymbol{\nabla} \cdot (\rho \mathbf{u}\mathbf{u}) = -\boldsymbol{\nabla} \cdot (p\boldsymbol{\delta}) + \boldsymbol{\nabla} \cdot \boldsymbol{\tau}, \tag{2.35}$$

where $\boldsymbol{\delta}$ is the unit tensor. Note that Equation 2.35 neglects viscous and nonlinear terms. Assuming the shock is planar, the pressure gradient becomes.

$$\frac{\partial p}{\partial x} \approx 0, \tag{2.36}$$

$$\frac{\partial p}{\partial y} \approx 0, \tag{2.37}$$

$$\frac{\partial p}{\partial z} \approx \frac{\partial \rho w}{\partial t}, \tag{2.38}$$

where the shock normal and the interface normal are in the z-direction.

Once inserting Equations 2.36 – 2.38 into Equation 2.34 we get,

$$\frac{\partial \omega_x}{\partial t} \approx -\frac{1}{\rho^2}\frac{\partial \rho}{\partial y}\frac{\partial \rho w}{\partial t}, \tag{2.39}$$

$$\frac{\partial \omega_y}{\partial t} \approx -\frac{1}{\rho^2}\frac{\partial \rho}{\partial x}\frac{\partial \rho w}{\partial t}, \tag{2.40}$$

$$\frac{\partial \omega_z}{\partial t} \approx 0. \tag{2.41}$$

If the shock accelerates the interface to a velocity V_0 and the density in each region is constant, Equations 2.39 - 2.41 become

$$\omega_x \approx \frac{V_0}{\rho}\frac{\partial \rho}{\partial y}, \tag{2.42}$$

$$\omega_y \approx \frac{V_0}{\rho}\frac{\partial \rho}{\partial x}, \tag{2.43}$$

$$\omega_z \approx 0. \tag{2.44}$$

For a 2D interface, then $\omega_x = 0$. This leaves equation 2.43, indicating that vorticity deposition can be shown using the density field and the nominal post-shock interface velocity in Figure 2.3. The strength of the pressure or density gradients, and how they are misaligned with the interface, determine the amount of vorticity that is deposited on the interface. This mechanism is present in the non-linear RT instability. In the RT instability, vorticity will be gradually generated when the pressure gradient opposes the density gradient, leading to instability and possibly inducing turbulence [17, 19].

2.5 Turbulence

Turbulence in the fluid regime has been studied quite prolifically in the fluid regime for well over century and has produced a multitude of definitions across a wide range

of subfields of physics [6, 19, 20, 23, 24, 25]. Dimotakis describes the transition to turbulent mixing in 3 stages: entrainment, stirring, and molecular mixing. Entrainment involves the introduction of large-scale, coherent eddies into a fluid. These eddies induce the stirring stage and amplify concentration gradients. Finally, the gradients enhance viscous and diffusive forces, leading to turbulent dissipation and molecular mixing.

Despite the range of definitions, scientists agree on several characteristics that define turbulent flows. Turbulence is diffusive. Turbulence is dissipative. Turbulent kinetic energy passes from large eddies to small eddies, sliding down what is known as the energy cascade until it reaches lengths scales small enough that it is dissipated into heat by viscous effects. As such, to accurately describe a system as turbulent the system must have the full spectrum of length scales.

2.5.1 Length Scales

There is a broad range of length and time scales that exist within a turbulent flow. Dimensional analysis provides insight into pertinent time and length scales. Fully-developed turbulent flows require a Reynolds number that is sufficiently high [23]. Given a length scale, L, and a velocity scale, u, the Reynolds number is simply the ratio of the inertial terms and the viscous terms, resulting in:

$$Re = \frac{uL}{\nu}, \tag{2.45}$$

where ν is the kinematic viscosity. We can now use the Reynolds number to determine the range of scales produced in the flow. The largest characteristic length scales (like L), are bound by the geometric dimensions of the flow. Fluctuating eddies within this flow have a length scale of λ with velocity scale $u(\lambda)$. The larger eddies obtain their energy from the bulk flow but then break apart into smaller and smaller pieces until they are small enough where viscous effects dominate and turbulent kinetic energy is dissipated into heat.

From observation, eddies lose most of their energy after one or two overturns. This indicates that the KE transfer rate ϵ from the large eddies to smaller eddies is proportional to their initial kinetic energy times their rotational frequency. Knowing that KE is proportional to velocity squared and rotational frequency is proportional to velocity over length, we find that the dissipation rate is:

$$\epsilon \propto \frac{u(\lambda)^3}{\lambda}. \tag{2.46}$$

This is simple, but has several implications. One is that the rate of dissipation is independent of the fluid's viscosity. Conversely, the length scale where this dissipation occurs is dependent on fluid viscosity. This length-scale is the infamous Kolmogorov length-scale, λ_K. The Kolmogorov length-scale is where viscous effects dominate and KE is dissipated into heat. We can continue using dimensional analysis to find the Kolmogorov length-scale by relating the dissipation rate to the kinematic viscosity from Equations 2.45 and 2.46 to obtain a unit of length,

$$\lambda_K \propto \left(\frac{\nu^3}{\epsilon}\right)^{1/4}. \tag{2.47}$$

We can continue with dimensional analysis to determine the time,τ, for the eddies to form, and velocity, v, of the smallest eddies formed:

$$\tau_K \propto \left(\frac{\nu}{\epsilon}\right)^{1/2}, \tag{2.48}$$

and

$$u_K \propto (\nu\epsilon)^{1/4}. \tag{2.49}$$

Note that inserting this velocity and length scale into the equation for the Reynolds number yields $u_K\lambda_K/\nu = 1$. Since the Reynolds number is the ratio of inertial to viscous effects, this relation supports that when viscous terms are relevant, turbulence does not occur. We can also find that the ratio of the smallest to the largest scales is:

$$\frac{\lambda_K}{L} \sim Re^{-3/4}. \tag{2.50}$$

Before discussing the additional length scales found in turbulent flows it is helpful to first discuss the energy cascade.

2.5.2 Energy Cascade

The energy spectrum, commonly interchangeable with power spectrum, of a turbulent system characterizes the turbulent kinetic energy distribution as a function of a length scale. It is usually described and shown in terms of wavenumber, k although it is commonly discussed as a length scale. The spectrum is able to show the amount of turbulent kinetic energy contained at each length. The process where the large

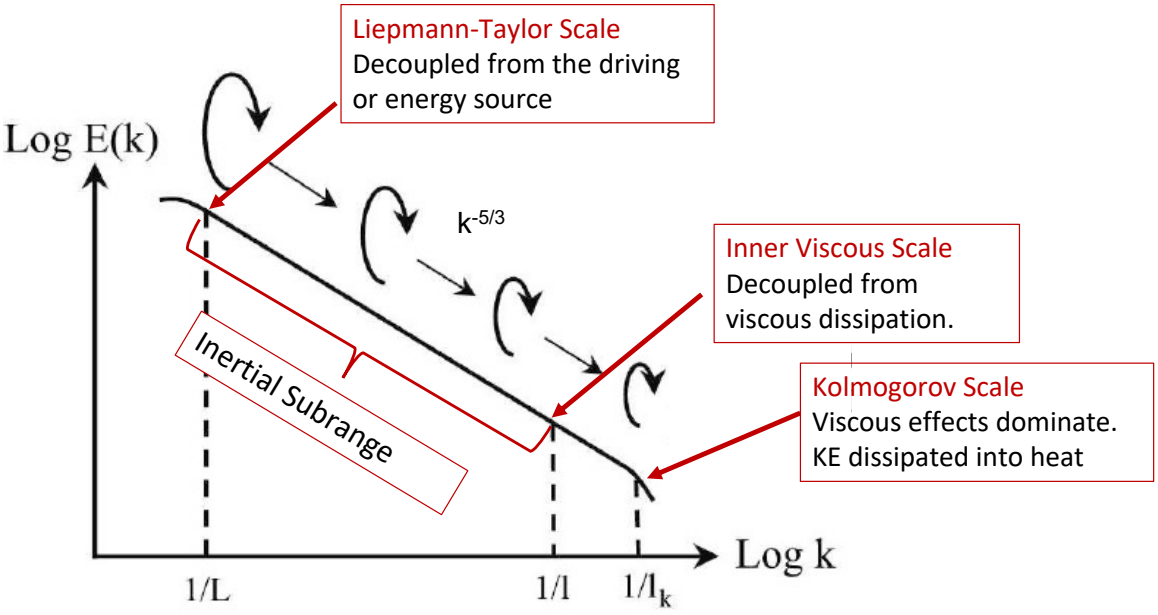

Figure 2.5: In the energy cascade, energy is transferred from large-scale eddies to smaller-scale eddies through a process known as "eddy breakup." As the energy is transferred to smaller scales, it is eventually dissipated by viscous forces within the fluid. Figure adapted from [21].

length scales transfer the energy to the next smallest scale is referred to as the energy cascade. Figure 2.5 shows the energy spectrum as a function of wavenumber with relevant length scales that will be discussed [19, 21, 22, 24, 23].

This region where the energy cascade occurs is referred to as the inertial subrange. It is bound by the Liepmann-Taylor length scale λ_{LT} and the inner-viscous scale λ_ν. The Liepmann-Taylor length scale denotes the lower limit of the energy-containing range where the the eddies draw energy from the mean flow and can be found using the thickness of a laminar boundary layer

$$\lambda_{\mathrm{LT}} = \frac{5\mathrm{L}}{Re^{1/2}}. \tag{2.51}$$

The eddies then break up into smaller and smaller pieces until they are small enough where viscous effects begin to dominate. The spectral energy density for each wavenumber within the inertial range is

$$E(k) \sim \epsilon^{2/3} k^{-5/3}. \tag{2.52}$$

The inner-viscous scale is the wavenumber where the energy spectrum begins to

deviate from the $k^{-5/3}$ power-law and is found by:

$$\lambda_\nu \cong 50\lambda Re^{-3/4}. \tag{2.53}$$

The flow within the inertial subrange is decoupled from both the driving source of the bulk flow and the viscosity. Length scales smaller than the inner-viscous scale are in the dissipation range, where turbulent kinetic energy is dissipated into heat.

2.5.3 Turbulence and Mixing

Turbulence can have an effect on fluid mixing. When a flow is turbulent, mass, momentum, and energy mix at a significantly more rapid rate than for a laminar flow. The type of mixing can be grouped into one of three categories. The first category occurs when a scalar (such as a dopant) is introduced into the flow and its mixing plays no role in the dynamics. The second category is when the introduced scalar does is affected by the fluid. The third category is when the scalar that is introduced in the flow becomes the dominant role in the behavior of the overall dynamics. Understanding when the flow has transitioned to turbulence is as important as what happens during turbulence [19].

As stated earlier, a flow in a turbulent state rapidly drives mixing. When in the turbulent state, mixing will lead to rapid dissipation of momentum and mixing at the molecular scale. The Kolmogorov theory [26] states that a flow has become turbulent when the inertial subrange begins to appear.

In HED physics we are interested in when flows achieve the minimum state. The minimum state describes the lowest Reynolds number necessary for an inertial subrange. This criteria is often used to diagnose the turbulent state used in many laboratory astrophysics experiments and is necessary to reproduce the dynamics within the energy-containing range [26, 27]. Dimotakis suggests that a flow has achieved this minimum state [19, 23] when the Reynolds number of a characteristic length-scale satisfies

$$Re \geq 10^4. \tag{2.54}$$

However, at $Re \sim 10^4$, the inertial scales and dissipation scales are just starting to separate and the inertial subrange does not yet exist. Therefore, the lowest Reynolds number should also provide a sufficiently long inertial range that allows for

a distinctive separation between the inertial and dissipative length scales. Robey et. al [22] determine the 'minimum state' where the Reynolds number allows the inertial subrange to appear and then diverge actually occurs when

$$Re \geq 10^5. \tag{2.55}$$

CHAPTER III

Crystal Backlighter Imaging

A common way to observe the instabilities in HED experiments is to probe a region of interest with an external source of x-rays to observe density distributions. X-ray diagnostics, such as pinhole imaging, have been used for many experiments conducted on OMEGA, OMEGA EP, and the NIF. Pinhole imaging is a well-known technique and can be coupled to either time-integrated or time-resolved detectors, in the HED regimes [28, 29]. However, pinhole imagers have a limited spatial resolution which is determined by the size of the pinhole. In order to collect enough signal, the pinhole must be relatively large in diameter, which can decrease the spatial resolution. For example, the area-backlit pinhole platform utilized by Flippo et. al and Nagel et. al on the NIF typically uses 25 μm diameter pinholes and a system magnification of 6x, resulting in a geometric resolution limit of ~ 29 μm [28, 29]. The length scales derived in Chapter II and utilized in Chapter IV are one to two orders of magnitude smaller than this. To set a pinhole diameter small enough to capture those length scales would reduce the brightness of the x-ray source and limit the number of photons detected [30]. The remainder of this Chapter discusses the physics behind a spherically-bent crystal imager, the diagnostic utilized in both experiments described in this thesis.

Multi-keV x-ray imaging coupled with a concave crystal x-ray mirror is a valuable diagnostic in the HED field. Bent-crystal microscopes provide a high signal-to-noise ratio (SNR), high spatial resolution image over a cm-size field of view (FOV) by backlighting or imaging the target's self emission. The experiments presented in this thesis utilize the bent-crystal microscopes installed on OMEGA, OMEGA EP, and the NIF [30, 31].

3.1 Spherical crystal imager resolution

X-ray imaging with bent crystals rely on the Bragg diffraction of x-rays from crystal planes. Only x-rays that satisfy the Bragg condition are reflected by the crystal lattice [32]. The Bragg condition is:

$$E = \frac{mhc}{2d\sin\theta}. \tag{3.1}$$

Here E is the x-ray energy, m denotes the reflection order, hc is the Planck constant times the speed of light, d is the lattice spacing, and θ is the angle of incidence, typically between 80° and 90°.

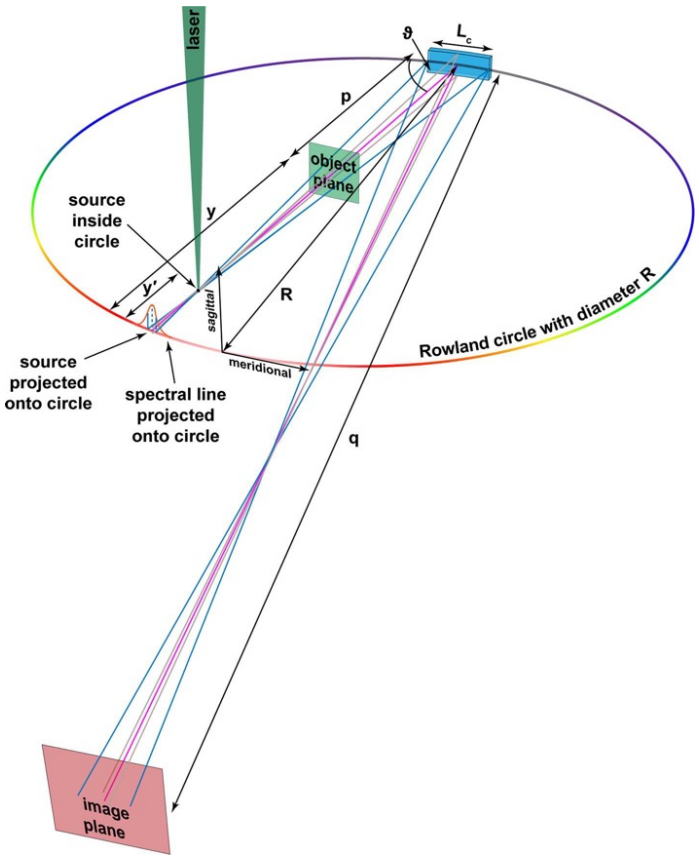

Figure 3.1: Schematic of a generic backlighter system using a spherically bent crystal with aperture L_C and a laser-created x-ray source inside the Rowland circle [33].

Figure 3.1 shows the Rowland circle, a circle where the diameter is the length of the radius of curvature, R, of the grating, such that

$$R_{\text{Rowland}} = R/2. \tag{3.2}$$

The generic cyrstal backlighter system typically lies on the Rowland circle and the image formation is described by Coddington's equations

$$\frac{1}{p} + \frac{1}{q_m} = \frac{2}{R_m \sin\theta}, \tag{3.3}$$

$$\frac{1}{p} + \frac{1}{q_s} = \frac{2\sin\theta}{R_s}, \tag{3.4}$$

where p is the object distance from the crystal, q_m and q_s is the image distance from the crystal in the meridional and sagittal plan, respectively, and R_m and R_s are the bending radii [34]. The diagnostic system is astigmatic meaning that the meridional and saggital focal lengths are different. To reduce the astigmatism in either foci, the object is placed at

$$p = \frac{R}{2}\frac{M+1}{M}, \tag{3.5}$$

where $M = q/p$ is the image magnification and the image distance q is given by

$$q = \frac{R}{2}(M+1). \tag{3.6}$$

Using these positions for p and q, the spatial resolution for the meridional and sagittal directions are effectively equivalent and is described by

$$\sigma = L\left(\frac{M+1}{M}\right)(1-\sin\theta). \tag{3.7}$$

Note that this indicates the spatial resolution deteriorates quickly as the object deviates from a normal ($\theta \sim 90$).

3.2 Image Fluence

Image fluence, also referred to as fluence rate or simply just fluence, is a measure of the amount of light or other electromagnetic radiation that falls onto a surface. It is typically expressed in units of energy per unit area, such as joules per square meter ($\mathrm{J/m^2}$). Image fluence refers to the amount of light that is captured by a detector. A higher image fluence indicates that more light was captured, which can result in a brighter and more detailed image. Therefore, one of the benefits of the spherical crystal diagnostic over the pinhole imager is that the image fluence is not limited the diameter of the pinhole.

In the context of this diagnostic, the image fluence I is given by the number of

photons per square micron. The fluence at the detector I_d (Equation 3.8) is dependent on the magnification, M, the crystal reflection coefficient, η, the number of photos, N emitted by the source, the crystal collection solid angle, Ω, and the area at the object plane A_{obj}. It is shown by the equation:

$$I_d = \frac{\eta N \Omega}{4\pi M^2 A_{obj}}. \tag{3.8}$$

3.3 X-ray sources

Laser-produced x-rays are generated by irradiating a metal foil with a high-energy laser beam. The intense energy of the laser beam excites the electrons in the metal atoms, causing x-ray emissions as as they return to their lower energy states. These x-rays can then be used for radiographic diagnostics. It is important to understand the process by which laser-produced x-rays are formed in order to effectively use them in diagnostic applications.

The laser intensity used to irradiate the backlighters for diagnostic purposes is typically in the range of 10^{13} to 10^{17} W/cm^2. Below 10^{13} W/cm^2, there is not enough energy density to initiate the x-ray production process. Above 10^{17} W/cm^2, relativistic effects start to occur, which can impact the dynamics of the process [5, 30]. The nominal laser intensity used on the backlighters in this case is approximately 10^{15} W/cm^2 for a long pulse laser [31].

Traditional x-ray sources typically involve accelerating electrons to high speeds and then bombarding a metal target with them in an x-ray tube. The impact of the electrons on the metal target can knock electrons out of the inner shells of the atoms, creating vacancies that are then filled by electrons transitioning from higher energy levels. This process releases x-rays with well-defined frequencies corresponding to the energy differences between the atomic energy levels of the target atoms. The line-emissions produced by transitions form the n=2 to n=1 levels are from the K_α x-rays and the n=3 to n=1 transitions are called He$_\alpha$.

Short pulse lasers ($<$ 500 ps) using chirped pulse amplification [35] are used to produce short duration K$_\alpha$ sources and long-pulse lasers ($>$ 500 ps) are used to produce longer duration He$_\alpha$ like sources. The time-scale of the x-ray source can determine the temporal resolution of the diagnostic.

3.4 Crystal Backlighter Imagers at experimental facilities

Facility	Crystal	Energy	Backlighter	Res.	Mag.	Detector
NIF	Silicon	11.652 keV	Se	7 μm	10x	IP
NIF	Mica	7.206 keV	Co	7 μm	10x	HGXD
OMEGA EP	Quartz	8.048 keV	Cu	$<$10 μm	10x	IP
OMEGA EP	Quartz	6.151 keV	Mn	21 μm	15x	CCD

Table 3.1: Each facility uses a different combination of crystals and backlighter materials that satisfy the Bragg equation. This table highlights the specifications for the crystal backlighter imagers discussed in this thesis [30, 31, 34, 33].

Spherical crystal imagers have been used to study HED physics for some time. These imagers used in this thesis are known as the Spherical Crystal Imager (SCI) and the Crystal Backlighter Imager (CBI) [31, 30, 28]. The SCI diagnostic is located at the OMEGA EP laser facility at LLE, while the CBI diagnostic is used at the LLNL's National Ignition Facility. Each facility uses a different combination of spectral-line crystals that satisfy the Bragg equation. Table 3.1 lists the type of crystal, their corresponding energy, the resolution at each facility, and the detector. The detectors consists of either a imaging plate (IP), the Hardened Gated X-ray Diagnostic (HGXD), or a charged-coupled device (CCD) [30, 36, 37, 38, 39].

CHAPTER IV

Experiments to Study Rayleigh-Taylor Instabilities on the NIF

The contents of this Chapter consist of two separate, yet related, campaigns: the VoRTex and the High Resolution Turbulence (HRT) campaign. The goal of the VoRTex campaign was to significantly advance the understanding of turbulent mixing within the Rayleigh-Taylor rollup region by adapting a well-characterized target system to the newly built spherical crystal microscope on NIF. The Director's Reserve proposal was submitted by Channing Huntington and executed by Sabrina Nagel. My initial contribution to this experiment was to understand and quantify the relevant turbulent length scales in our the RT unstable NIF experiment, understand the photometrics of the CBI diagnostic, and optimize the new target given the earlier statements. Following the success of the VoRTex experiment, the HRT campaign sought to further improve the resolution of the platform and provide proof-of-principle turbulent vortex measurements. The first half of this Chapter covering the experimental design was published in the *Journal of Instrumentation* [40]. The HRT campaign was originally led by Louisa Pickworth with a team that included Gareth Hall, Alexandre Do, Sabrina Nagel, Harry Robey, and myself. Between 2019 and 2022, I acted as the HRT campaign designer (under Harry Robey's and Chris Weber's guidance) by performing HYDRA simulations that informed target designs and diagnostic optimization for 8 NIF shot days. Simulations and analysis discussed for the remainder of the Chapter were published in *Physics of Plasmas* by Alexandre Do [37]. We conclude that while the system was still unable to directly measure turbulent-relevant length-scales, the experimental resolution of the system improved 3-fold.

4.1 Introduction

Late-time, nonlinear Rayleigh-Taylor (RT) unstable behavior plays a key role during multiple phases of inertial confinement fusion (ICF) capsule implosions [5, 12, 29, 41, 42, 43, 44]. Imperfections present on the capsule interface cause mixing that cools the hot spot which reduces the fusion yield. As the RT instability develops, the cold, dense material (spikes) interpenetrates the hot, less dense material (bubbles) and cools the system. However, the present diagnostic resolution ($\geq$7 μm) is larger than the RT spikes present in ICF-relevant length scales ($\leq$ 3 μm). Due to these diagnostic limitations, it is difficult to diagnose the dynamics that occur along the spike tip and ascertain whether mixing alone is present, or if the system transitions to turbulence. Simulations are one method to study this mixing behavior, but it is difficult to model fine-scale structures. It is computationally expensive to directly resolve the range of spatial and time scales necessary to diagnose mixing or turbulence. Reduced model simulations remove small-scale information and use numerical schemes to model small-scale effects on broader dynamics. Simulations performed with with identical initial conditions, but different numerical schemes generate different structures [45, 46] and, therefore, require experiments to validate these models.

Numerous experiments have been conducted at LLE and the National Ignition Facility that were aimed at measuring the nonlinear RT growth using x-ray radiography (Figure 4.1) [29, 47, 18]. Yet these platforms were optimized at measuring the gross mix width of the instability, and not the fine-scale features that develop along the spike tip. Facility and diagnostic advancements allow us to reach regimes and image features that may play a significant role in HED RT-unstable systems.

4.2 Turbulence-relevant length scales in HED

A hydrodynamic system is considered RT unstable when a density gradient opposes a pressure gradient ($\nabla\rho \cdot \nabla P < 0$). In a system where a heavy fluid is accelerated into a light fluid, the contact surface is unstable and small perturbations initially present on the surface begin to grow [48, 49]. Imposing a single-mode sine function of known wavelength and amplitude on the interface seeds the instability and enables a less-complicated description of how the penetrating heavy fluid (spikes) and light fluid (bubbles) evolve through various stages [20, 50]. Figure 4.2 highlights spikes and bubbles in a previous HED, single-mode RT unstable experiment [29].

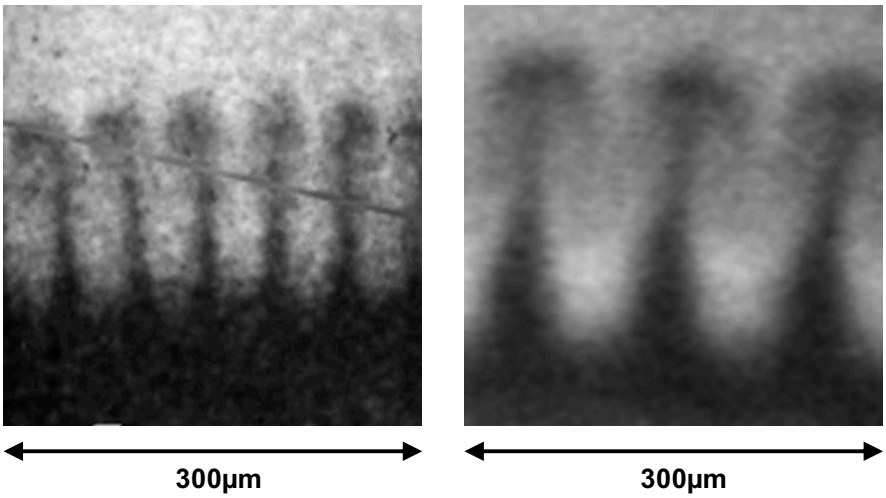

Figure 4.1: X-ray radiographs of RT instability structure obtained by Robey et. al [41] on the Omega Laser in 2001 (left) and Nagel et. al [29] on the NIF in 2016 (right). Targets with a larger initial wavelength (right) produce larger, more visible vortex features.

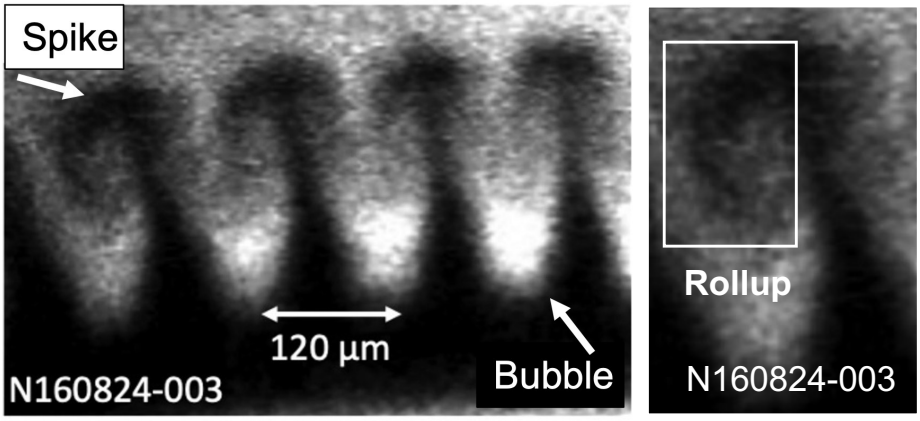

Figure 4.2: As the RT instability develops, the cold, dense material (spikes) interpenetrates the hot, less dense material (bubbles) and cools the system. Rollups form along the RT spike tip [29, 37].

As the instability further evolves and the amplitude grows to approximately 10 percent of the wavelength, it approaches the early nonlinear stage [18, 21]. Figure 4.3 shows an evolution of this process. It is during this stage that nonlinear terms become large enough to make significant contributions to the interface features that affect the growth rate [18, 22]. Vorticity, the curl of the velocity, is introduced as the density gradient becomes misaligned from the pressure gradient along the length of the spike in Equation 2.33. It creates vortex features that cause the spike to broaden as it grows. It is also possible that the vorticity induces a transition to turbulence within this vortex feature, however this is not a guaranteed result [20].

Figure 4.3: Growth and saturation of the Rayleigh-Taylor instability, observed by acceleration of two fluids in a test facility performed by Jacobs et. al [20]. Classical fluids experiments that seek to define turbulence in RT unstable experiments are able to achieve larger length scales (millimeters) for a longer time (microseconds) than HED experiments.

Turbulence has been studied quite prolifically throughout the century and has produced a multitude of definitions across a wide range of subfields of physics [5, 21, 23, 24]. Fundamental turbulence theory defines turbulence as (i) the development of substantially convoluted structure at an interface, having spectral content or spatial extent far beyond those of the initial state, (ii) the appearance of an inertial range in the fluctuation spectrum, with power-law decay of the spectral energy density, and (iii) the development of strong mixing as indicated by supra-linear growth of the thickness of the mixing layer in time [5].

However, the experiment described in this chapter highlights the practical aspect of understanding and diagnosing turbulence as it applies specifically to HED physics and to ICF. Therefore, we claim our system is transitioning, or has transitioned, to turbulence if the Reynolds number reaches the 'minimum state' described in Chapter II ($Re \geq 10^5$) [5, 18, 21, 23, 24, 47]. To refresh the reader's mind of Equation 2.45, the Reynolds number is the ratio of inertial forces to viscous forces used to classify the

type of flow and is described as $Re = uL/\nu$. If the Reynolds number is low, viscous effects are apparent, and the flow is considered laminar. If the Reynolds number is high, viscous effects are minimal or nonexistent, and the flow is turbulent.

A method to experimentally ascertain that the system has reached Re $\sim 10^5$ is to resolve spatial scales corresponding to the Liepmann-Taylor scale, $\lambda_{\mathrm{LT}} = 5\mathrm{LRe}^{-1/2}$ [21, 51, 19]. The λ_{LT}, or inertial range, is an intermediate length scale at which the fluid is decoupled from small-scale fluid viscosity and large-scale bulk dynamics. So, length scales which are larger than λ_{LT} are not strongly affected by viscosity. Conversely, turbulent motions below λ_{LT} are dominated by viscous forces and kinetic energy is dissipated into heat [23, 47]. Additionally, the appearance of λ_{LT} is one of the definitions of turbulence discussed earlier. Figure 4.4 shows the resulting Liepmann-Taylor scale as it relates to the Reynolds Number and HED-laboratory length scales. The region in parameter space where the experiments in this thesis exist is highlighted by the red box.

4.3 Experimental Design

This experimental design utilizes a similar laser conditions and physics package from previous successful campaigns conducted on the NIF [29, 47]. This experiment is conducted in a rectangular shock tube and is driven by a holhlraum on one end. When the halfraum (described in Chapter I) is irradidated with the laser, it produces a thermal bath of soft x-rays that generates a strong shock into a physics package comprised of high-density plastic and low-density foam. The strong shock turns this initially solid target into a plasma and the material boundary between the plastic and foam becomes a fluid interface. The high-density fluid (plastic) is accelerated into the low-density fluid (foam) and the system becomes RT unstable. A precise single-mode sine pattern is machined at the fluid interface to seed the RT instability with a known amplitude and wavelength such that it will achieve a sufficient degree of nonlinearity during the experiment. After a specified time delay, additional lasers will irradiate a foil to produce the hard x-rays necessary to radiograph the evolving interface.

4.3.1 Laser Parameters

The main laser parameters for this experiment is the same that was used in ReShock campaign described in Nagel et. al [29]. The laser pulse is generated by

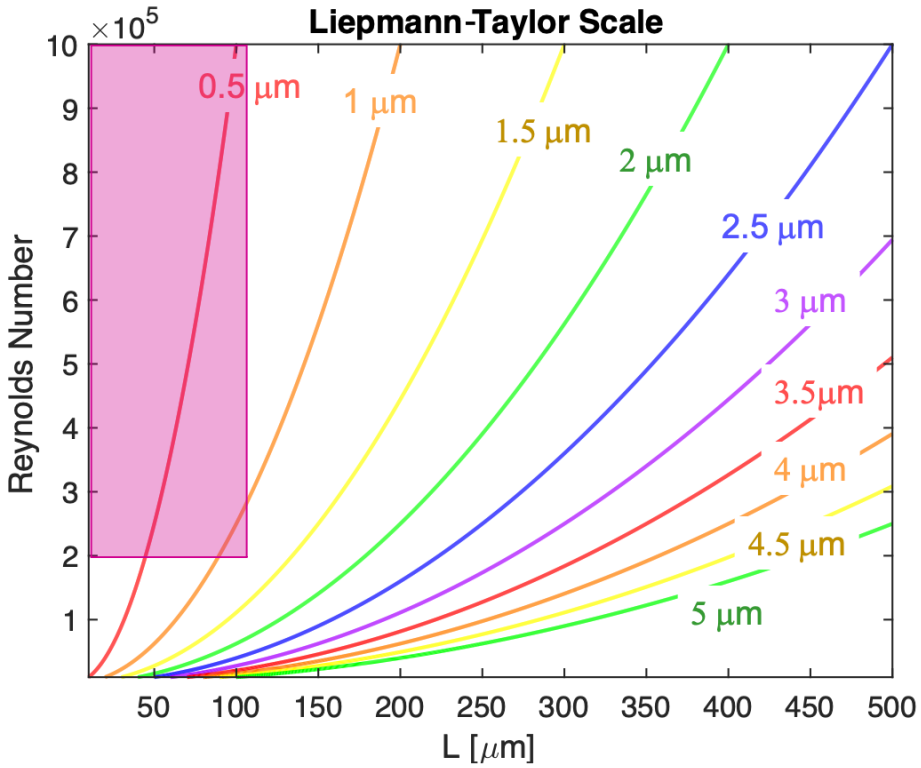

Figure 4.4: The Liepmann-Taylor scale as it relates to the Reynolds Number and HED laboratory length scales (L) where $L_{\mathrm{LT}} = 5LRe^{-1/2}$. The region in parameter space where the experiments in this thesis exist is highlighted by the red box.

60 NIF beams in two stages. The first stage has a peak power of 35 TW that is maintained for 3 ns. It is followed by the second stage when the peak power linearly ramps down to 15 TW over another 3 ns before ending. The beams are pointed towards the laser entrance hole (LEH), located approximately 5.6 mm above the target center. To obtain the radiograph at a chosen time, the backlighter is driven by an 8.8 TW laser pulse from 4 beams with a 400 μm diameter. The backlighter material differs with each shot to produce different x-ray energies due to the process described in Section 3.3.

4.3.2 The Physics Package

The high density component, or ablator, involves two density-matched (1.43 g/cm^3) plastics: polyamide-imide (PAI), $C_{22}H_{14}N_2O_3$, and an iodine-doped polystyrene (CHI), $C_{50}H_{47}I_3$. Models and previous experiments suggest that the plastics behave hydrodynamically similar [29], but the CHI is relatively opaque to the imaging x-ray energy compared to the PAI. Therefore, a 300 μm thick slice of CHI is placed at the center

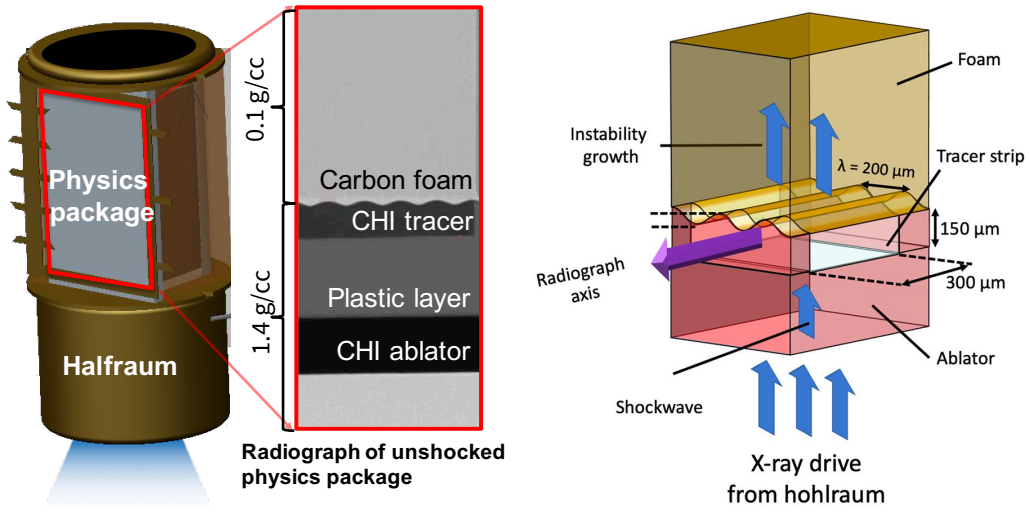

Figure 4.5: (Left) A schematic of the target package consisting of the halfraum and physics package adapted from Nagel et. al [29]. The x-ray drive from the halfraum launches a shock into the physics package that accelerates the dense plastic into the lighter foam, inducing an RT unstable interface. A red line highlights and borders the pre-shot radiograph of the physics package. (Right) An exploded 3-dimensional view of the physics package shown by Do et. al [37]. The heavy plastic has a doped, 300 μm thick tracer to enhance the contrast solely at the center of the target.

of the PAI to act as a tracer strip. This improves the contrast between the plastic and foam, and reduces multi-dimensional effects. The ablator compound is machined with a sinusoidal perturbation on the plastic-foam interface wavelength $\lambda = 200$ μm and an initial sinusoidal amplitude (a_0) of $a_0 = 7.5$ μm and 15 μm (with peak-to-valley amplitudes, a_{PV}, of $a_{\mathrm{PV}} = 15$ μm $a_{\mathrm{PV}} = 30$ μm) respectively for two separate targets. Figure 4.5 shows an exploded view drawing of the physics package. In the image, the lasers irradiate the halfraum generating an x-ray bath that ablates the plastic and drives a shock that propagates through the physics package [29]. The shock accelerates the high density CHI ablator, PAI layer, and CHI tracer into the low density CRF foam, creating an RT unstable interface.

According to the criteria for nonlinearity described above, growth rates and dynamic structure begin to deviate from classical linear theory when $a_0/\lambda \sim 0.1$. The initial conditions set on this platform obtain an initial a_0/λ ratio of 0.037 and 0.075 respectively and the experiment already begins in the weakly nonlinear regime. Radiographs of previous NIF experiments confirm that the perturbations grow into the deeply nonlinear regime by about halfway through the $\sim$ 60 ns experiment [29, 47].

Figure 4.1 (Right) shows that the interface has evolved from the sinusoidal initial condition (λ =120 μm and a_0 = 6 μm), and has entered the nonlinear regime by 46 ns after the initial laser drive.

The spike tips display mushroom cap features characteristic of the late-time RT behavior, which was the goal of the VoRTex experiment. Increasing the wavelength from λ =120 μm to λ = 200 μm increases the spacing between the spike tips and mitigates any possibility of the spike mergers. To compensate for the large wavelength while maintaining the same non-linearity, the initial amplitudes in the VoRTex campaign are increased to a_0 = 7.5 μm and 15 μm to not only increase the size of the features, but to compensate for the increased wavelength in the amplitude-to-wavelength ratio. The spike tip features in Figure 4.1 (Right) are notably indiscernible at the 28 μm spatial resolution, and a higher resolution x-ray diagnostic is required to diagnose the dynamics within that region.

4.4 Pre-shot modeling and simulated radiographs

Using the characterization of the CBI instrument described above we are able to produce 'synthetic radiographs' by post-processing 2D simulations with the appropriate resolution and noise properties of the instrument. I created the 2D simulations for this exercise using the radiation hydrodynamics code HYDRA [52, 53]. HYDRA is a multi-physics simulation code from LLNL, that is used to simulate a variety of experiments carried out at NIF. HYDRA can simulate radiation transfer, atomic physics, hydrodynamics, laser propagation, and a number of other physics effects [53]. Figure 4.7 shows a series of synthetic radiographs of the pre-shot HYDRA simulations and is discussed in further detail later in this chapter.

4.4.1 Pre-shot Drive Calibration

Radiation hydrodynamic simulations use a time-dependent radiation temperature source (referred to as the 'drive'). The radiation temperature source is applied to the plastic material boundary to induce a shock that traverses through the perturbed surface and into the lower density material.

The drive for pre-shot simulations were initially calibrated against separate NIF experiments (shot N170322) performed by Nagel et. al [29]. The experiment utilized

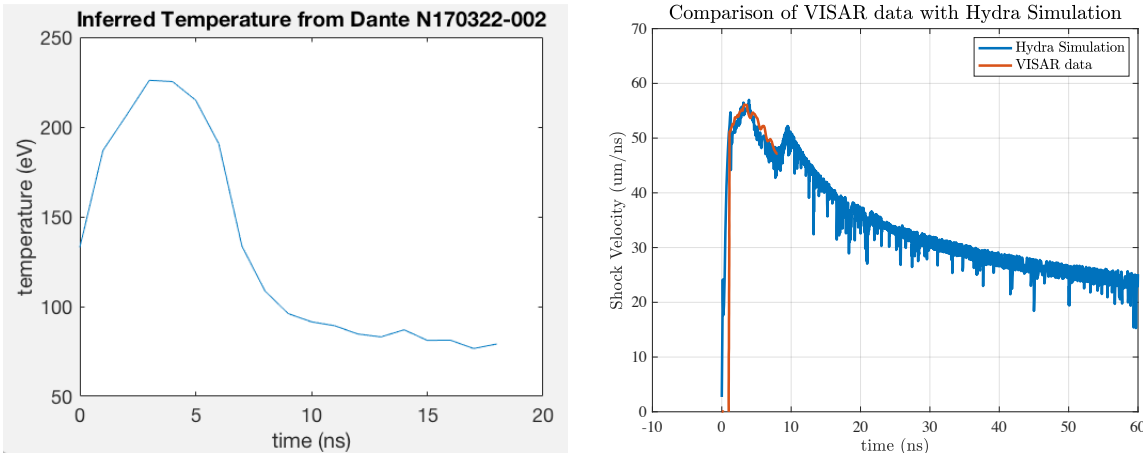

Figure 4.6: (Left) The halfraum temperatures (Tr) as a function of time (ns) inferred from Dante for a similar shot day (N170322) is used as the temperature source for the HYDRA simulation [29]. Th(Right) The temperature for the drive is tuned with a time-dependent multiplier until the resulting shock velocities align [29].

the velocity interferometer system for any reflector (VISAR) diagnostic [54] and the Dante diagnostic [55]. Dante is a broadband, soft x-ray spectrometer that measures the total x-ray flux, conversion efficiency, and radiation temperature [55]. The left image in Figure 4.6 shows the temperature source from Dante that drives the physics package for N170322. The VISAR diagnostic relates the shock velocity to the driver conditions [29, 54].

The pre-shot simulations utilize the halfraum temperature obtained from Dante as the drive. The resulting simulated shock velocity is then benchmarked against the shock velocity measured by VISAR. The drive is then adjusted by a time-dependant multiplier until the simulated shock velocity aligns with the measured shock velocity. Figure 4.6 shows the simulated shock velocity of the calibrated drive. An iterative list time-dependent drive multipliers is found in Appendix B.

The 2D hydrodynamic simulation modeled a planar slice through the target, and we account for the third dimension–the axis parallel with the radiograph vector by assuming that the 2D slice represents the material profile along this axis throughout the target. We assume that non-planarity has a negligible impact on the measurement since the contrast in the x-ray radiograph is sensitive almost exclusively to the 300 μm CHI doped tracer strip. These details are not resolvable in the limit of the 2D approximation for radiographs with the 7 μm resolution of the CBI. Therefore, further

loss of image fidelity around the smallest-scale features of the image does not change our conclusions with the present platform.

Figure 4.7 shows the x-ray transmission, I, through the 2D simulation output. The x-ray transmission calculation uses the map of material (plastic and foam) location at each point (x, y), and the density at each point, $\rho(x, y)$. The transmission fraction $I(x, y, E)$ for a given x-ray energy, E, is calculated for each pixel of the synthetic radiograph according to:

$$I(x, y, E) = I_0 \prod_i e^{(-\rho(x,y)_i \times \sigma(E)_i \times l_i)}, \tag{4.1}$$

where σ is the mass attenuation coefficient, l is the thickness of each material, and the subscript i designates each of the materials along the x-ray line of sight. The length of foam (l_{foam}) is 1900 μm in the 2D map of material. Where the simulation indicates that there is plastic, it is assumed that there is 1600 μm of PAI (l_{PAI} = 1600 μm) and 300 μm of CHI (l_{CHI} = 300 μm) along the line of sight. The mass attenuation coefficient, σ, depends only on the material and the x-ray energy, E [8]. All the synthetic radiographs in Figure 4.7 calculate the transmission of the material based off the 9 keV x-ray energy used for previous experiments, except the when post-processing for the CBI setup, which calculates the transmission using the 11.6 keV x-ray energy used for the CBI.

A qualitative comparison between the existing data can be made by artificially degrading the x-ray transmission image according to the diagnostic characteristics. The pinhole camera used to produce the data in Figure 4.7 has been shown to have an image resolution of approximately 27 μm (full-width-half-max point spread function) [29]. The simulations produced in Figure 4.7 show the result of performing a Gaussian blur of this magnitude that represents the diagnostic resolution, and imposing a level of Poisson noise to represent the signal noise at the scale of the image plate resolution element (25 μm), to the ideal image. Though the structure is not exact, this synthetic pinhole camera image is qualitatively similar to the experimental data. Note that the data was collected at 9.0 keV [29]. We can apply the same processes with the imaging parameters of the CBI, namely a FWHM resolution of 7 μm (the same magnitude of image-plate Poisson noise was applied). Although the fine details in the vortex regions at the spike tip and along the spike are still below the resolution limit, the improvement is significant.

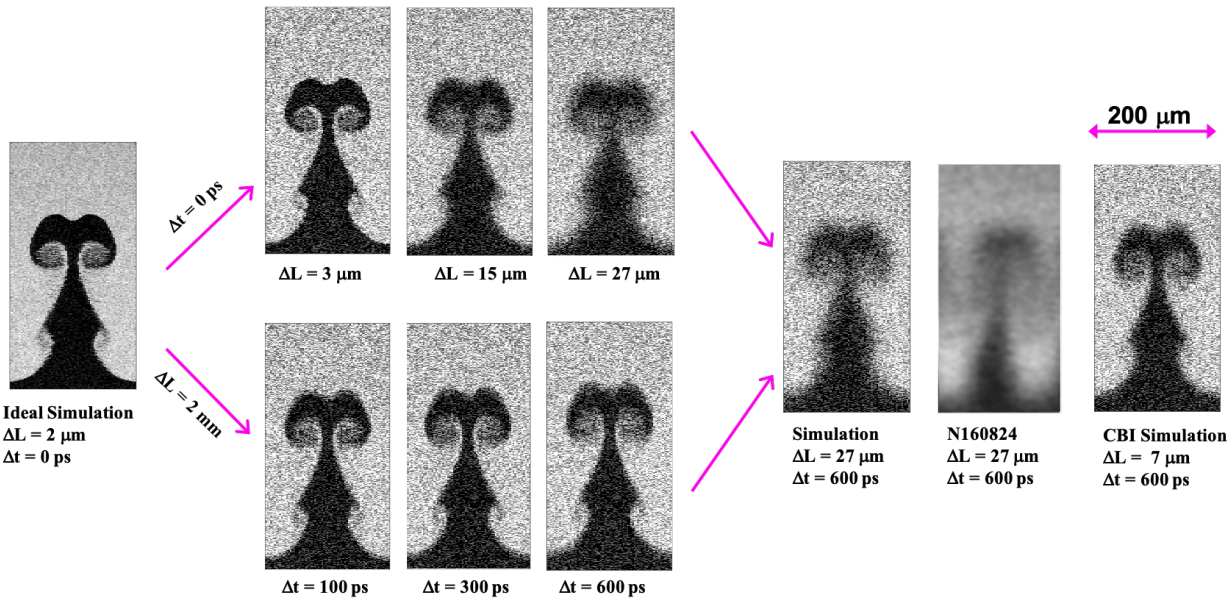

Figure 4.7: This figure shows a series of synthetic radiographs based on post-processed 2D simulations, assuming a monochromatic 9 keV x-ray energy, systematically degraded spatially and temporally until the synthetic radiograph is comparable to data taken with the pinhole imager and what is achievable with the CBI. The ideal simulation has a spatial resolution (ΔL) of 2 μm and temporal resolution (Δt) of 0 ps. The figure then bifurcates where the top series of synthetic radiographs sets the temporal resolution as constant ($\Delta t = 0$) while the spatial resolution degrades, and the bottom series sets the spatial resolution constant ($\Delta L = 2$ μm) while the temporal resolution degrades. The top row shows the effect of the various diagnostic capabilities on the experimental resolution. The bottom row shows the contribution of motion blur and therefore the importance of moving to a shorter integration time (Δt). This converges into a synthetic radiograph emulating the pinhole imager conditions, example data from shot N160824-003, and finally a synthetic radiograph emulating CBI conditions. The CBI simulation incorporates the 11.6 keV x-ray energy in addition to the temporal and spatial resolutions listed above. The synthetic radiographs were post processed with blur (ΔL = FWHM) and Poisson noise.

4.5 Experimental Results

A series of shot days were performed on the NIF to simultaneously commission the CBI and study the formation of the RT spikes under different initial Atwood numbers. Table 4.1 summarizes the initial conditions of the VoRTex and HRT campaigns. The listed time describes the timing of the backlighter pulse relative to the onset of the laser drive. The wavelength and sinusoidal amplitude describe the single-mode machined perturbation on the plastic-foam interface. The sinusoidal amplitude to wavelength ratio is chosen such that they are already near the weakly nonlinear regime, according to the nominal criterion $a_0/\lambda \sim 0.1$. The initial Atwood number, A_0 is calculated from the initial plastic density, $\rho_{\text{plastic}} = 1.45$ g/cm^3, and the initial foam density ρ_{foam} listen in the table. Figures 4.8 and 4.9 show radiographs from the VoRTex (N190213) and HRT (N200809) campaign, respectively. These two radiographs were taken with the CBI at different times, with different initial foam densities, or a different backlighter material that produce different x-ray energies. In these images, the shock is incident from the bottom of the images and travels vertically upwards. All the targets have a wavelength $\lambda = 200$ μm and plastic density $\rho_{\text{CHI}} = 1.45$ g/cm^3.

Variable	VoRTex	HRT
time	46 ns	50 ns
λ	200 μm	200 μm
a_0	15 μm	20 μm
a_0/λ	0.075	0.1
ρ_{foam}	85 mg/cm^3	145 mg/cm^3
A_0	0.89	0.81

Table 4.1: Parameters describing the initial conditions of the VoRTex and HRT campaigns. The listed time describes the timing of the backlighter pulse relative to the onset of the laser drive. The wavelength and sinusoidal amplitude describe the single-mode machined perturbation on the plastic-foam interface. The sinusoidal amplitude to wavelength ratio is chosen such that they are already near the weakly nonlinear regime, according to the nominal criterion $a_0/\lambda \sim 0.1$. The initial Atwood number, A_0, is calculated from the initial plastic density, $\rho_{\text{plastic}} = 1.45$ g/cm^3, and the initial foam density ρ_{foam} listed here.

Figure 4.8 shows an experiment with an initial foam density $\rho_{\text{CRF}} = 85$ mg/cm^3 and initial sinusoidal amplitude $a_0 = 15$ μm. A 600 ps backlighter pulse irradiated a Se foil to produce 11.6 keV x-rays onto an image plate at t = 46 ns. The shock front

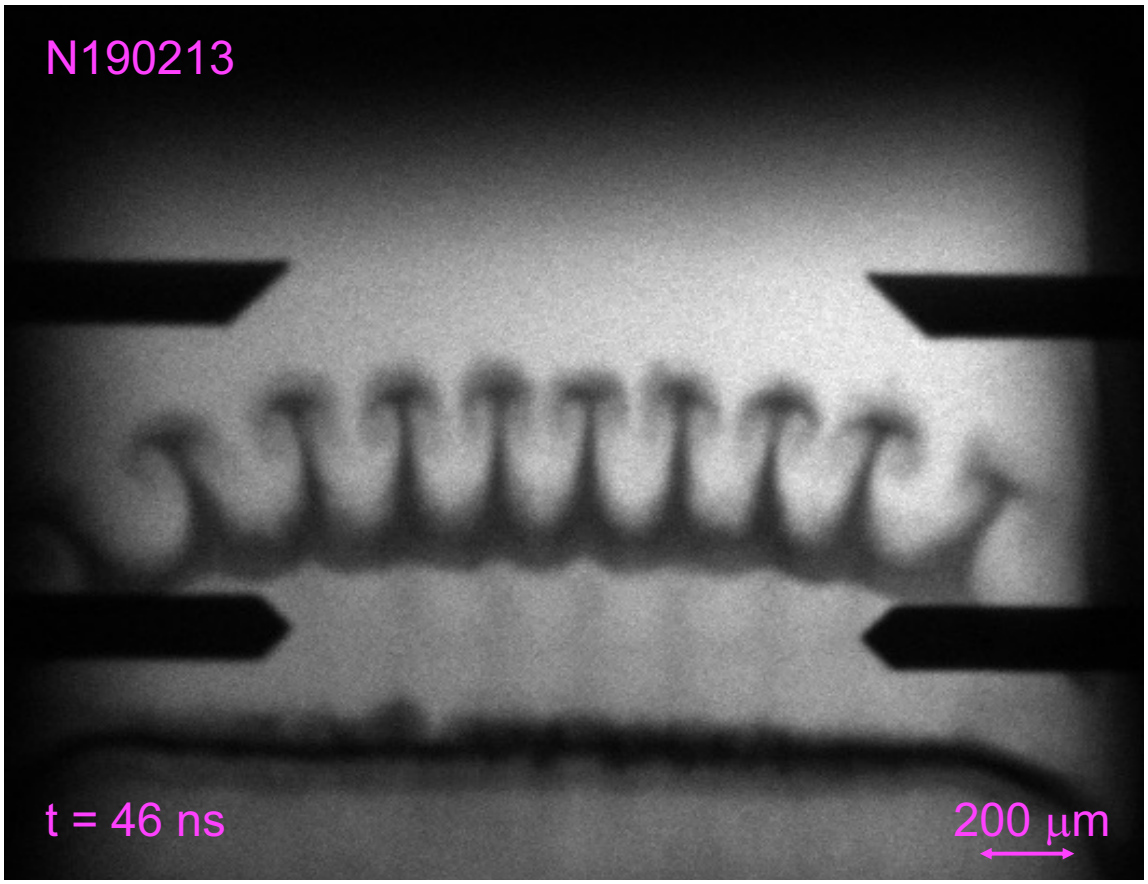

Figure 4.8: Experimental radiograph N190213 from the VoRTex campaign. The shock is incident from the bottom of the images and travels vertically upwards. The initial foam density is $\rho_{\mathrm{CRF}} = 85$ mg/cm^3, $\rho_{\mathrm{CHI}} = 1.45$ g/cm^3, and initial sinusoidal amplitude $a_0 = 15$ μm. A 600 ps backlighter pulse irradiated a Se foil to produce 11.6 keV x-rays onto an image plate at t = 46 ns.

is difficult to see in this image due to the poor contrast between the shocked and unshocked foam for this backlighter energy. Simulations calibrated to the experiment (discussed later in this Chapter) show that the material velocity is ~ 40 μm/ns. This indicates that the temporal blur due to the temporal gating is ~ 24 μm. The experimental spatial resolution is found using the following equation:

$$\delta_s = \sqrt{\delta_{\mathrm{CBI}}^2 + \delta_{\mathrm{blur}}^2 + (\delta_{\mathrm{det}}/M)^2}, \tag{4.2}$$

where δ_s is the experimental spatial resolution, δ_{CBI} is the resolution of the diagnostic, δ_{blur} is the resolution from the temporal blur, δ_{det} is the spatial resolution of the detector, and M is the magnification [28]. By inserting the aforementioned values in Equation 4.2, we find that the experimental resolution for shot N190213 is ~ 29 μm.

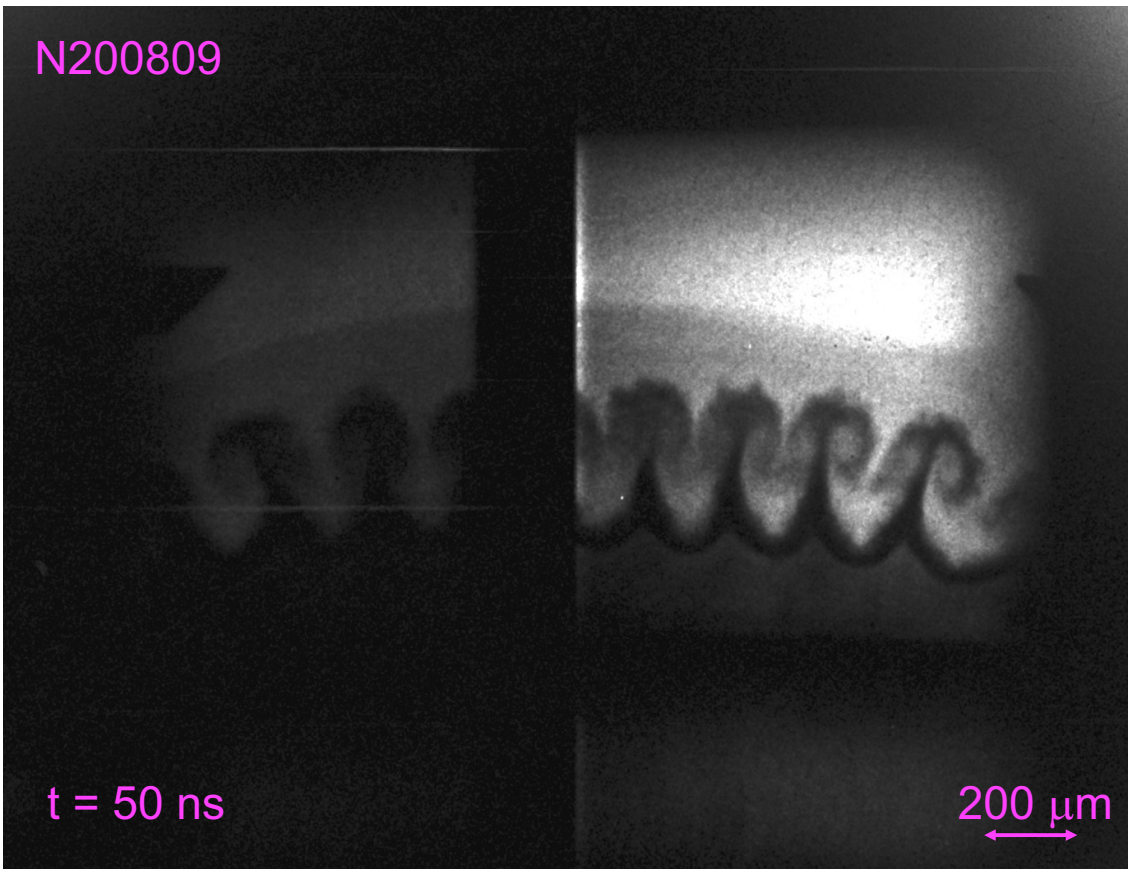

Figure 4.9: Experimental radiograph N200809 from the HRT campaign. The shock is incident from the bottom of the images and travels vertically upwards. The initial foam density is $\rho_{\mathrm{CRF}} = 145$ mg/cm^3, $\rho_{\mathrm{CHI}} = 1.45$ g/cm^3, and initial sinusoidal amplitude $a_0 = 20$ μm. A 100 ps backlighter pulse irradiated a Co foil to produce 7 keV x-rays onto the 2 strip HGXD at t = 50 ns. The black strip in the middle is an image artifact from the HGXD [39, 56].

Figure 4.9 shows the radiograph from the HRT campaign (N200809) with an initial foam density $\rho_{\mathrm{CRF}} = 145$ mg/cm^3 and initial sinusoidal amplitude $a_0 = 20$ μm. A backlighter pulse irradiated a Co foil to produce 7 keV x-rays onto a gated HGXD (described in Chapter III)[29] at t = 50 ns for 100 ps. The lower backlighter energy allows for greater contrast due to the x-ray transmission described in Equation 4.1. The shock front in N200809 is now visible. Due to the higher foam density, the material velocity has now slowed to 30 μm/ns. This, coupled with the 100 ps gate time indicates the fluid will move 3 μm, therefore produces a motion blur of 3 μm. The experimental resolution for shot N200809 is 9 μm, but the higher foam density has induced more prominent rollups along the RT spike and possibly even secondary KH structures along that interface. Table 4.2 summarizes the improvements

between the Reshock, VoRTex, and HRT campaigns. The experimental resolution for the HRT campaign improved four-fold from the Reshock campaign and three-fold from the VoRTex campaign. The improvement was achieved by shortening the backlighter pulse, reducing the material velocity in the physics package, and lowering the backlighter energy on the CBI.

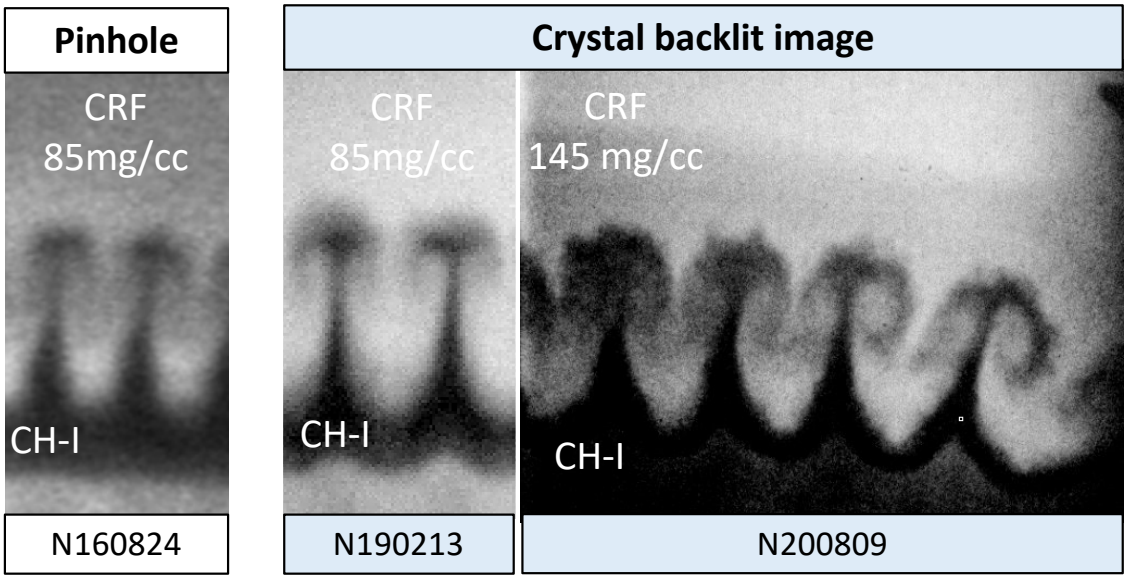

Figure 4.10: Target and diagnostic changes improved experimental resolution 3-fold. Adapted from Do et. al [37].

The vortical rollups that appear at the tip of the spikes are the regions of interest where the flow is most likely to become isotropic. On the other hand, N200809 started with a higher initial amplitude and a higher foam density, causing the rollup to become more pronounced. The later imaging time of N200809 allows the hydrodynamics to evolve and match those of the earlier-in-time N190213.

4.6 Spectral Analysis

An indication that the flow has transitioned to turbulence is the appearance of the inertial subrange. Of the three radiographs discussed, N200809 had the highest resolution and the most prominent rollups. Data shown in Figure 4.11 from N200809 is spectrally analyzed to reveal information about the density fluctuations in the rollup.

Parameter	Reshock	VoRTex	HRT
Spatial resolution	28 μm	8 μm	9 μm
Temporal resolution	600 ps	600 ps	100 ps
Material velocity	40 μm/ns	40 μm/ns	30 μm/ns
Temporal blur	24 μm	24 μm	3 μm
Backlighter energy	9 keV	11.6 keV	7 keV
Experimental resolution	39 μm	29 μm	9 μm
Diagnostic	Pinhole	CBI	CBI
Detector	Image Plate	Image Plate	HGXD

Table 4.2: Parameters describing the target and diagnostic improvements between the Reshock, VoRTex, and HRT campaigns. The experimental resolution for the HRT campaign improved four-fold from the Reshock campaign and three-fold from the VoRTex campaign. The improvement was achieved by shortening the backlighter pulse, reducing the material velocity in the physics package, and lowering the backlighter energy on the CBI.

Several steps are required to determine the power spectrum of the image. First several regions of interest (ROI) are decided on and cropped from the figure. The red box in Figure 4.11 corresponds to the vortex region with the highest likelihood of isotropy and turbulence. The typical size of the ROI was kept consistently at 50 μm x 50 μm so only the rollup is considered. The power spectra of the radiograph is extracted by using a two-dimensional fast Fourier transform (FFT). We are able to do so directly from the x-ray intensity fluctuations because they are directly related to density fluctuations [57, 58]. This also implies that the density fluctuations should behave as a passive scalar that is transported with the flow. The 2D-power spectra is then projected onto polar coordinates and averaged over all angles to obtain an average radial power spectrum [57, 58]. This process was repeated for an ROI in the unshocked region shown in the blue square in Figure 4.11 to compare spectral characteristics between the two regions.

The amplitude of the spectra from the signal region (red) are higher than that of the background (blue), indicating that the measured fluctuations are due to the driver/foam interface, and not the shocked foam. However, the fact that the slopes are approximately equal shows that the density fluctuations are in the same energy driving range. This suggest that the λ_{LT} scale was not resolved and confirms that the experimental resolution limit did not capture the turbulent length scale. However, post-shot modeling can provide further insight into the dynamics of this region with the Reynolds number calculation.

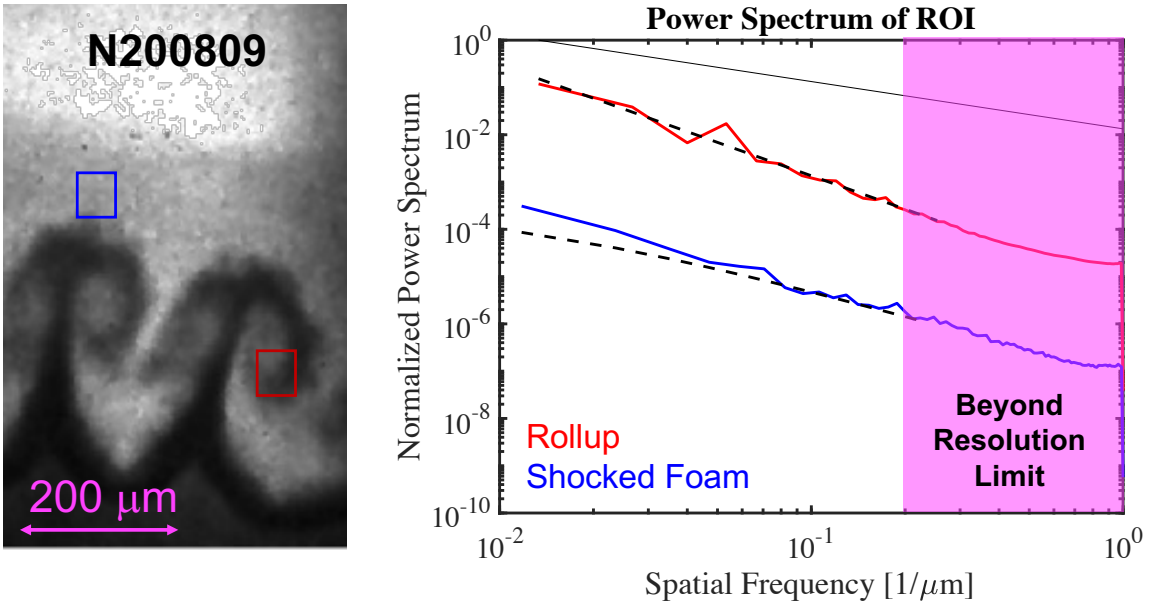

Figure 4.11: (Left) Region of interest from an x-ray radiograph from the HRT campaign (N200809). Darker regions highlight the dense, high-opacity pusher material. The square denote regions used for analysis of the isotropic region (red) and the shocked foam (blue). (Right) Calculated normalized power spectra are shown for both analyzed regions with their respective fits marked by the dashed line. The magnitude of the spectra from the rollup region is higher than the shocked foam region, indicating that the measured signal is dominated by the driver/foam interaction.

4.7 Post-shot modeling and discussion

Although the inertial subrange is not resolvable with the improved diagnostic techniques, it is still useful to compare the resulting radiographs with simulations to validate modeling at a detailed level. Doing so allows us to determine various physical parameters (temperature, density, pressure, fluid velocity, viscosity) which could not be experimentally determined. I calibrate the simulations to the experiment by comparing their interface positions, the mix-widths, and shock positions. To achieve this, I iterated over a series of radiation temperature sources, number of radiation groups, and mesh sizes until the metrics of interest were converge.

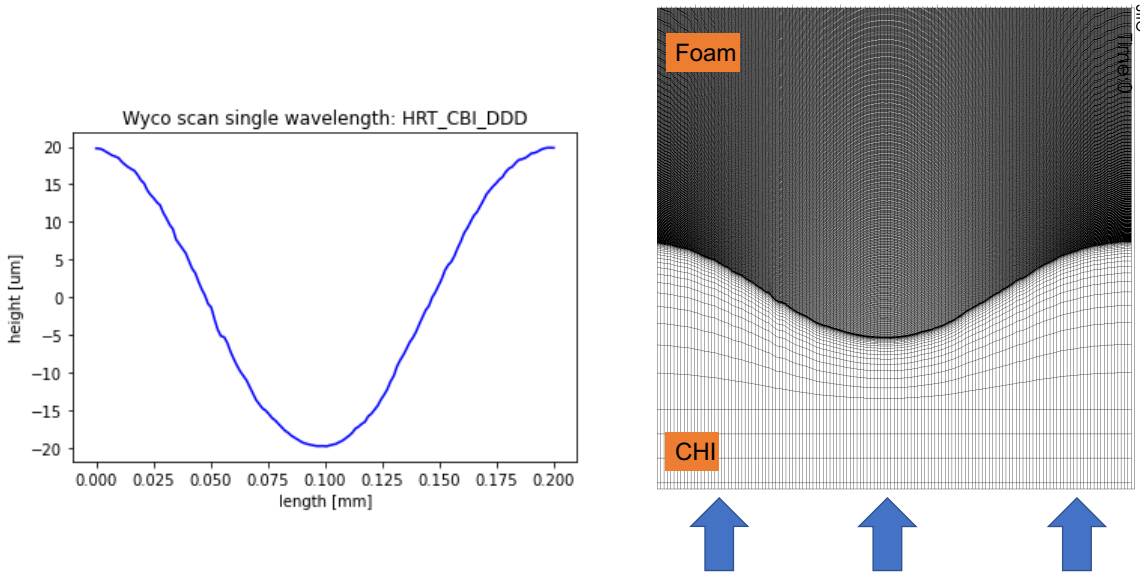

Figure 4.12: (Left) HYDRA's initial condition used to simulate shot N200809. The perturbation is a measurement of the surface perturbation from the target shot for N200809 using the WYCO microscope scanner at General Atomics [59]. (Right) The 2D mesh generated for the N200809 HYDRA simulation. The mesh resolution is $\sim$ 1.4 μm resolution along the length. The mesh height gradually transitions from 3 μm at the CHI material boundary to 0.5 μm as it approaches the CHI/Foam interface, becoming uniformly spaced at the interface. The source is applied to the CHI material boundary to induce a shock the at traverses through the perturbed surface and into the lower density material.

I further refine the initial drive temperature used for pre-shot modeling (described in Section 4.4.1) to reflect the experimental conditions and more accurately inform future days. Figure 4.12 shows the initial conditions and mesh used to simulate shot N200809. The initial conditions used to simulate shot N200809 is a direct measurement of the surface perturbation from the exact target used for N200809 using the

WYCO microscope scanner at General Atomics [59]. The 2D mesh generated for the N200809 HYDRA simulation. The mesh width is uniformly ~ 1.4 μm. However, the mesh height gradually transitions from 3 μm at the CHI material boundary to 0.5 μm as it approaches the CHI/Foam interface, becoming uniformly spaced at the interface. The source is applied to the CHI material boundary to induce a shock the at traverses through the perturbed surface and into the lower density material.

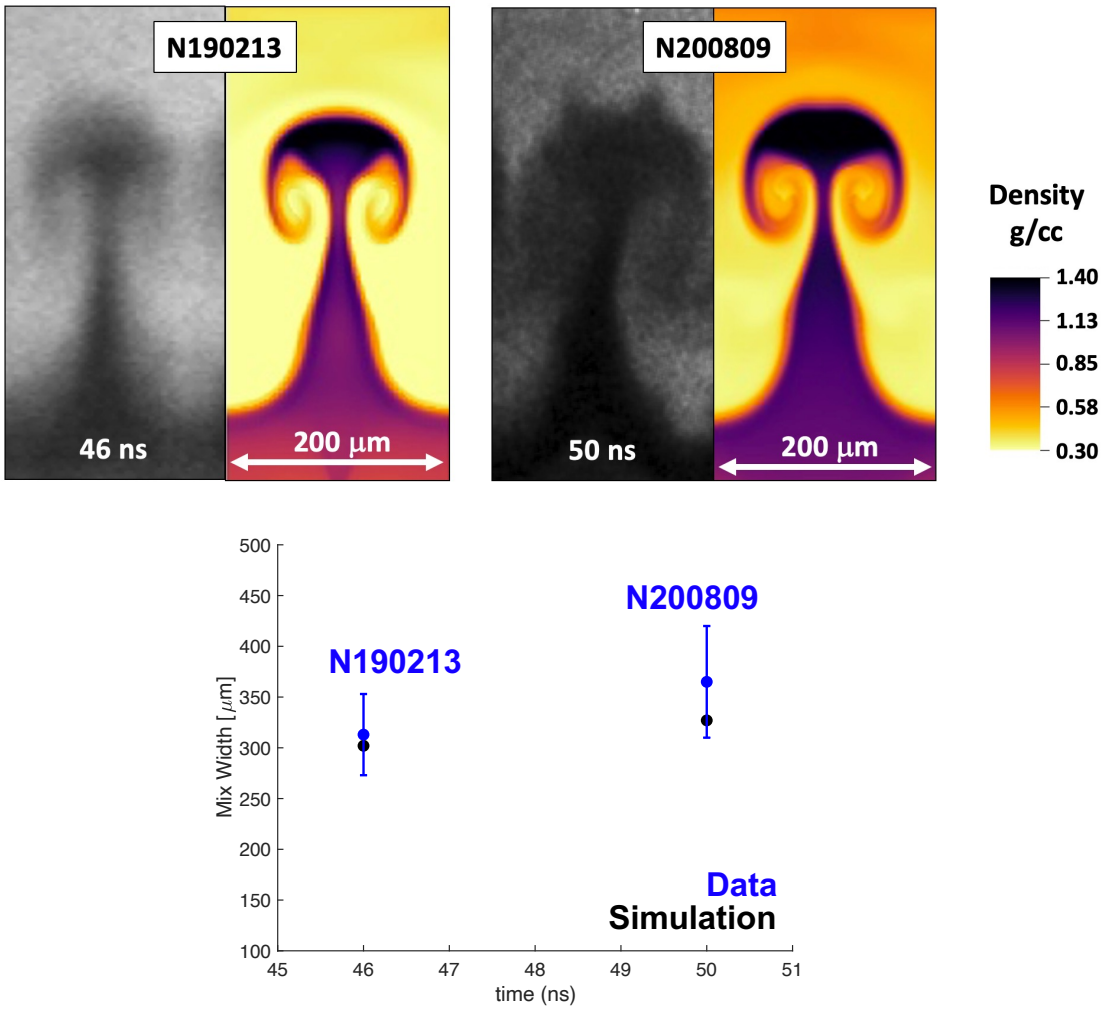

Figure 4.13: Simulation and experimental mix-width comparison for N190213 and N200809. The simulated mix widths lie within the resolution limit. It is interesting to note the similarity of the mix-widths between the two shot days despite their differing times and initial foam densities (see Table 4.1).

Figure 4.13 compares the simulation mix-width to the experimental mix-width and quantifies the plots. The simulated mix widths lie within the margin of error for

the experiment. The margin of error is determined from Equation 4.2 as well as using the 10% - 90% edge measurement. To get this measurement, a lineout is taken along the mushroom tip, the maximum and minimum points are identified. The result is the number of number of microns spanning between the points that are 10% and 90% of the maximum value. The two shot days are share similar mix-widths despite their initial foam densities because the HRT shot was given more time for the dynamics to evolve before the image was taken.

4.7.1 Determining the Reynolds number

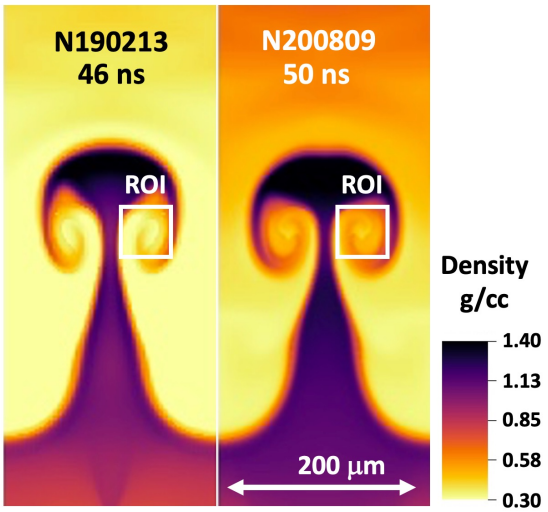

Figure 4.14: HYDRA density output of shot N190213 and N200809 showing highlting the ROI utilized for Table 4.3.

Variable	VoRTex Sim	HRT Sim
u (μm/ns)	5.5 $\pm$ 1.5	4 $\pm$ 1
ν $\times 10^{-4}$ (μm^2/ns)	5 $\pm$ 4	7 $\pm$ 4
L (μm)	50 $\pm$ 5	50 $\pm$ 5
Re $\times 10^5$	5.5 $\pm$ 2.6	3.2 $\pm$ 1.8
λ_{LT} (μm)	0.43 $\pm$ 0.15	0.35 $\pm$ 0.06

Table 4.3: The extracted variables and resulting Reynolds numbers determined within the ROI shown in Figure 4.14. The energy injection length scale, L, is the size of the rollup. The velocity within the ROI describes transverse motion in order to remove effects from the bulk flow. The viscosity shown is the average viscosity found in the ROI. The λ_{LT} scale is determined from $\lambda_{\mathrm{LT}} = 5L/Re^{1/2}$ using the values L and Re listed here.

We can estimate the Reynolds number within the rollup region of interest from the 2D HYDRA simulation results. Figure 4.14 highlights the region of interest (ROI) from which we obtained the variables to calculate the Reynolds number. We choose our energy injection length scale L as the length of the rollup, and the velocity is estimated using only the transverse motion to remove effects from the bulk flow. HYDRA utilizes the Spitzer-Braginskii model to calculate the viscosity [52]. The Spitzer-Braginskii model is given as

$$\nu = 3.3 \times 10^{-5} \frac{\sqrt{A} T^{5/2}}{ln(\Lambda) Z^4 \rho_i}, \tag{4.3}$$

where ν is the kinematic viscosity in cm^2/s, T is the ion temperature measured in eV, ρ is the density in g/cm^3, A is the atomic weight, Z is the atomic number, and $\ln(\Lambda)$ is the Coulomb logarithm [47].

Table 4.3 shows the values extracted from the simulations and their resulting Reynolds number and Liepmann-Taylor scale. Both simulations result in Reynolds number of order 10^5 and satisfy the minimum state described by [19]. Both simulations also highlight that the resulting Liepmann-Taylor scale estimate is < 1 μm, so would not be resolvable in the current experimental data even if the system is transitioning to turbulence at the time it was imaged. Furthermore, because the LT scale is smaller than the simulation spatial resolution, spectral analysis would not observe this transition in the spectral shape.

4.8 Summary and Future Works

The VoRTex campaign aimed to experimentally diagnose the transition to turbulence in blast-wave-driven, RT-unstable, HED system. The HRT campaign sought to further improve the resolution with a series of target and diagnostic enhancements. The combined efforts of these two campaigns resulted in a 3-4 fold improved experimental spatial resolution from experiments that previously used pinhole images and produced the most detailed x-ray radiographs of late-time RT evolution and small-scale features at the NIF.

However, even with these improvements, the necessary spatial scales were not resolvable. Pre-shot and post-shot HYDRA simulations highlighted the importance

of reducing the motion blur. To do so, the initial foam density increased from 85 mg/cm^3 in the VoRTex campaign to 145 mg/cm^3 in the HRT campaign to slow down the mixing dynamics, while the temporal resolution was improved by reducing the backlighter pulse from 600 ps to 100 ps. Spectral analysis of the rollup and shocked foam in the radiograph from shot N200809 shows different magnitudes in the two regions. This indicates that there are discernible fluctuations between the two regions. However, neither region exhibit the $k^{-5/3}$ spectrum decay that would identify the existence of the inertial subrange and that post-shot simulations are necessary to determine if the rollup region meets the minimum-state Reynolds number criteria.

Table 4.3 shows the values extracted from the relevant HYDRA simulations that are necessary to calculate the Reynolds number and Liepmann-Taylor scale. According the simulated values, the minimum-state criteria for the Reynolds number is met for both N021319 and N200809. The resulting Liepmann-Taylor scales that exists within the rollup region exists is still an order of magnitude smaller than the diagnostic limit.

Future experiments interested in directly measuring the Liepmann-Taylor scales in an HED platform would benefit from a variety of alterations. For one, looking at a different region with a larger characteristic length scale would create larger, and possibly resolvable, Liepmann-Taylor scales. Figure 4.4 shows how the Liepmann-Taylor scale relates to the Reynolds number and length scale. A system with a larger energy-injection length scale L such as a KH-unstable platform, would yield a larger Liepmann-Taylor scale that might be detectable by the resolution capabilities of current diagnostics.

CHAPTER V

Experiments to Study Kelvin-Helmholtz Instabilities on OMEGA EP

The experiments described in this chapter is a laboratory astrophysics experiment to investigate the role of the KH instability in star forming galaxies. Graduate student Shane Coffing performed the hydrodynamic simulation that informed the experimental design and scaling as it relates to the astrophysical regime. This work is published in *The Astrophysical Journal* [60]. I executed the hydrodynamically-scaled experiments on the OMEGA EP facility and use the resulting radiographs to observe the dynamics behind filament collapse and KH evolution on the deflected surface. The supporting post-experiment, hydrodynamic simulations were performed by Matt Trantham on CRASH. The entirety of the raw data from both shot days described in this chapter, as well as the experimental set up page are shown in Appendix C.

5.1 Introduction

The Universe is a cosmic web comprising of filaments and galactic halos. Figure 5.1 shows the hot galactic halos interconnected by the filaments. Filaments are cold and dense 'cylindrical streams' of dark matter and baryons. Halos are 'spherical clumps' of dark matter and baryons in the center of which galaxies form. Galaxies grow by accreting gas from halos, and the stars that form within the galaxies are regulated by the availability of gas. In essence, the gas supply to a galaxy acts as a bottleneck for star formation and ultimately sets its star formation rate [1, 2, 62, 63].

Before delving further into galaxy formation, it is important to first discuss the virial theorem and its resulting components. The virial theorem relates the total kinetic energy, KE, of a relaxed and isolated self-gravitating body to roughly half

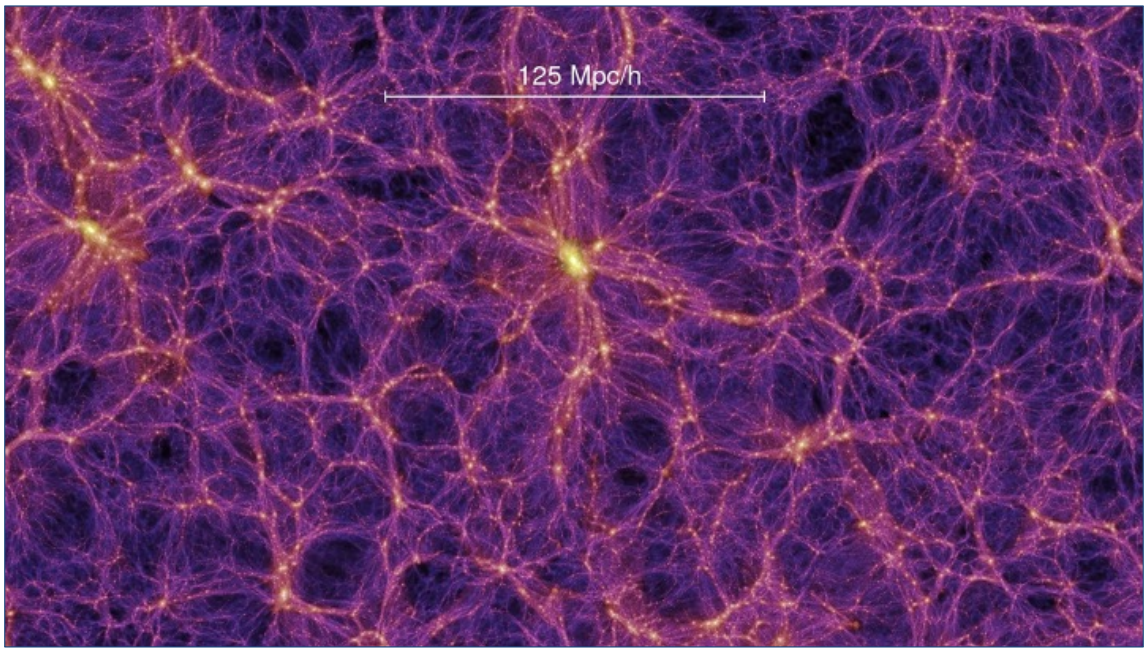

Figure 5.1: The Millennium Simulation is a large-scale computer simulation of the evolution of the Universe over a period of 13.7 billion years. It was carried out by a team of international scientists led by the Max Planck Institute for Astrophysics. The simulation was able to reproduce many of the observed features of the Universe, such as the distribution of galaxies in clusters, the formation of cosmic web-like structures, and the growth of large-scale structures through the process of hierarchical clustering. The results of the simulation have been used to study a wide range of astrophysical phenomena, including galaxy formation and evolution, the distribution of dark matter, and the impact of supermassive black holes on the evolution of galaxies [61].

the total potential energy, PE, therefore

$$KE = \frac{1}{2}|PE|. \tag{5.1}$$

By assuming $KE = Mv^2/2$ and $PE = GM^2/R$, the above equation becomes

$$M = \frac{v^2 R}{G}, \tag{5.2}$$

where M is the total mass of the galaxy, v is the mean velocity of matter in the galaxy, G is Newton's gravitational constant, and R is the effective radius of the galaxy which we refer to as the virial radius. We define the virial radius, R, of a gravitationally bound astrophysical system as the radius within which significant mixing of the infalling gas begins. For baryons, the infalling gas converts its kinetic energy into thermal energy by passing through a strong shock, the 'virial shock'.

Consequently, the virial temperature, T_V, is the baryonic component of the kinetic energy, and is the average temperature of the matter located within the virial radius [1].

Now back to our story.

Above the virial shock, the gas is 'cold', at roughly 10^4 K, set by an equilibrium of its cooling rate and photo-ionization by the intergalactic UV background radiation [64]. As the matter falls towards the center, it quickly becomes supersonic and various modes of behavior may occur depending on the virial mass of the halo [1, 2]. When the virial mass is below a critical value of $M_{crit}=10^{12}M_{\odot}$, the post-shock cooling rate is so large that the shock itself becomes unstable, and the infalling gas reaches the galactic center without passing through a shock (Filament mode). Above this critical temperature two scenarios can occur. At relatively low redshifts, the infalling gas is smooth and gets shocked at the virial radius to the virial temperature (Accretion mode). At higher redshifts, the infalling gas is sufficiently non-isotropic, with significant density variations in the direction of the filaments. Since the cooling rate scales as the density squared, in this situation the majority of the volume in the halo is expected to be at the virial radius, while the majority of the inflow is concentrated in the supersonic streams connected to the cosmic-web filaments (Dual mode) [1, 2, 65, 60]. Figure 5.2 shows a schematic of the three modes described above.

- Accretion mode: high-mass galaxy ($M_{\rm falling} > M_{\rm crit}$) in the hot regime, the infalling matter is shock heated and begins to fall supersonically. An accretion shock forms quickly, close to the virial radius, and far from the galactic center.
- Filament mode: low-mass galaxy ($M_{\rm falling} < M_{\rm crit}$) in the cool regime, the matter begins to clump into filaments that deliver mass to the galactic center to form stars. If a shock does form, it forms close to the galactic center.
- Dual Accretion/Filament Mode: High-mass galaxy ($M_{\rm falling} > M_{\rm crit}$) in the rapid cooling regime. Matter that had already formed into filaments are able to withstand the accretion shock located at the virial radius and penetrate deeply into the galactic center.

At low redshift ($z < 1.5$) there is a distinctively sharp transition from the hot to cold regime when sufficient mass has fallen through the filaments, such that the halo mass becomes greater than $M_{\rm crit}$ [2, 60]. However, large N-body cosmological

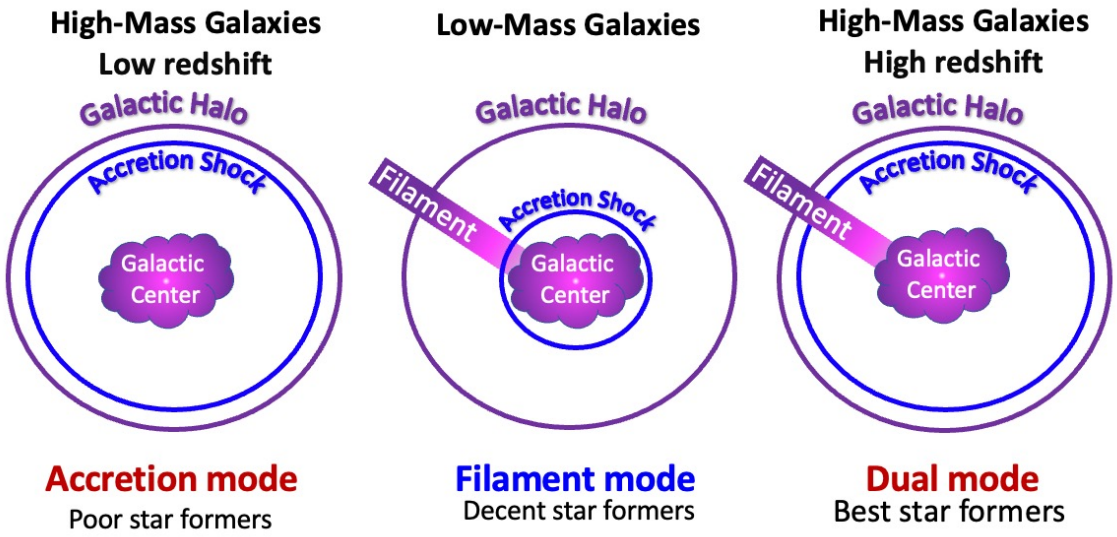

Figure 5.2: Rapid cooling galaxies with high mass are the most proficient star-formers due to filaments.

simulations indicate that at higher redshifts ($z > 1.5$), the gas flow within the filament is able to withstand the shock and maintain a terminal velocity from well outside the virial radius to deep within the halo [2]. Figure 5.3 shows the analytical predictions for each of the three modes as a function of redshift and mass. This indicates that there are additional processes present that reduce energy that would otherwise be gained from the galaxy's gravitational potential. In the case of a cold, dense stream in a hot, less-dense background, high shear velocities exist along the filament edge, thereby making it KH unstable [23, 62, 66].

Despite the likely existence of KH growth along the filament edges, there has been relatively little research on the hydrodynamic processes involved in the evolution of cosmic filaments. Recently, Padnos et. al [66] examined the potential impact of the KH instability on the structure of filaments through a combination of numerical and analytical analysis, but assumed idealized conditions for the halo-stream interactions, without the process of the stream penetrating through the virial shock. They found that under certain conditions, the KH instability could grow quickly enough to significantly affect the shape of the filament [66]. However, if a (virial) shock is present, the shock wave can be driven into the filament stream which could not only affect the KH evolution, but compress the filament and disrupt the stream entirely.

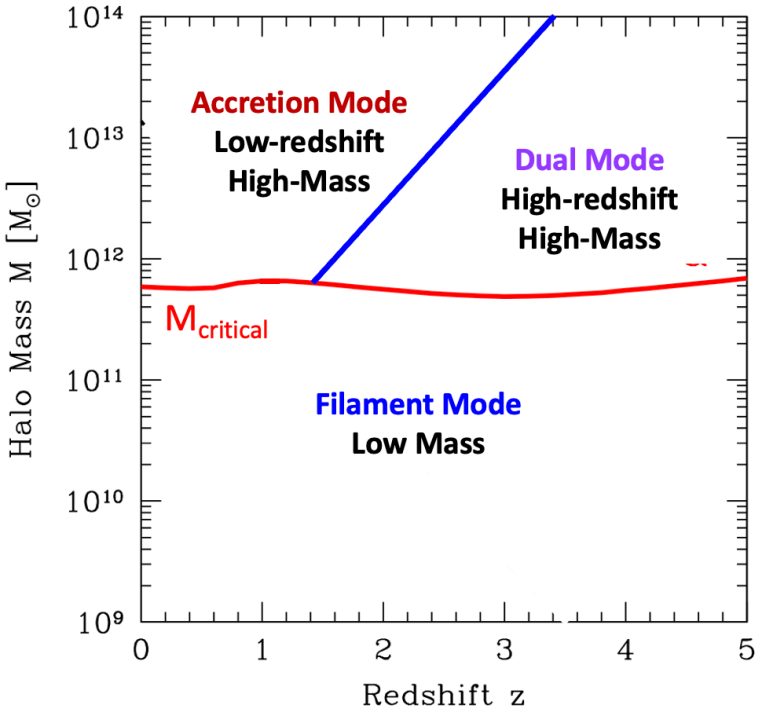

Figure 5.3: Analytic predictions for the modes dominated by cold flows shown in Figure 5.2 as a function of redshift (z) and mass. The nearly horizontal red curve marks the critical mass where the sharp mode transition occurs. Haloes below the critical mass are expected to have filaments while haloes above the critical mass will quickly form an accretion shock. Haloes above the cirtical mass and with redshift $z < 1.5$ are expected to be in the dual accretion/filament regime. Adapted from Dekel et. al [2].

Currently, the cosmological models that are able to resolve the cold streams and shocks can only simulate large-scale structures such as filament radii, mean densities, and flow velocities, but are not capable of accurately modeling the small-scale physics that occur along the boundary of the filament. Performing an experiment that is well-scaled to capture the small-scale physics of cosmic filaments as well as the virial shock can provide an upper limit on the impact of the KH instability in idealized situations, which can then be applied to the astrophysical case [2, 60].

5.2 Kelvin-Helmholtz Evolution

We are able to mimic the idealized galactic filament process by driving a shock through a scaled, cylindrical target designed for the OMEGA EP laser located at the Laboratory for Laser Energetics. The shock causes a cylindrical plastic rod, that acts as our filament, to flow through a shock-heated foam that acts as our background. The interface between the cold, dense stream (values with subscript s) in a hot, less-dense background (values with subscript b) is KH unstable [67].

The KH instability arises when a velocity gradient exists within a fluid or across the interface between two fluids. While this was previously discussed in Section 2.2, I will refresh the readers mind with theory relevant to this experiment. As the KH instability evolves, small perturbations located on the interface surface, or shear layer, form vortices that eventually cause mixing. In the linear regime of an incompressible flow, the amplitude of the perturbation on the interface, h, is expected to grow exponentially as $h \sim h_0 \exp(\gamma_{\rm ic} t)$, where h_0 is the initial amplitude and t is the time. Here, the incompressible growth rate, $\gamma_{\rm ic}$, is given by:

$$\gamma_{\rm ic} = \frac{k\Delta u}{2}\sqrt{1 - A^2}. \tag{5.3}$$

In this equation, $k = 2\pi/\lambda$ is the wavenumber, $\Delta u = V_s - V_{\rm b}$ is the difference between stream velocity ($V_{\rm s}$) and the background velocity ($V_{\rm b}$), and $A = (\rho_{\rm s} - \rho_{\rm b})/(\rho_{\rm s} + \rho_{\rm b})$.

However, if the fluid's density changes as a result of the pressure changes in the fluid, the system is described as a compressible flow, the KH instability will grow at

the rate:

$$\gamma_{\rm c} = \left[\frac{k\Delta u}{2}\sqrt{1-A^2}\right]\frac{\sqrt{-1-M_{\rm c}^2+\sqrt{1+4M_C^2}}}{M_{\rm c}}, \tag{5.4}$$

where $M_{\rm c}$ is the convective Mach number, $M_{\rm c} = \Delta u/(c_{\rm s}+c_{\rm b})$, and c_s and c_b are the sound speeds of the stream and background. We can choose a frame of reference such that the background is stationary, $V_{\rm b} = 0$, and the stream has velocity, $\Delta u = V_{\rm s}$, that is parallel to the stream-background interface. Then our convective Mach number becomes $M_{\rm b} = V_{\rm s}/c_{\rm b}$. The KH instability evolving on the deflected gas-filament interface is assumed to evolve in the linear, subsonic, compressible regime with the analytical growth rate shown in Equation 5.4 [60, 67].

5.3 Timescale Comparison

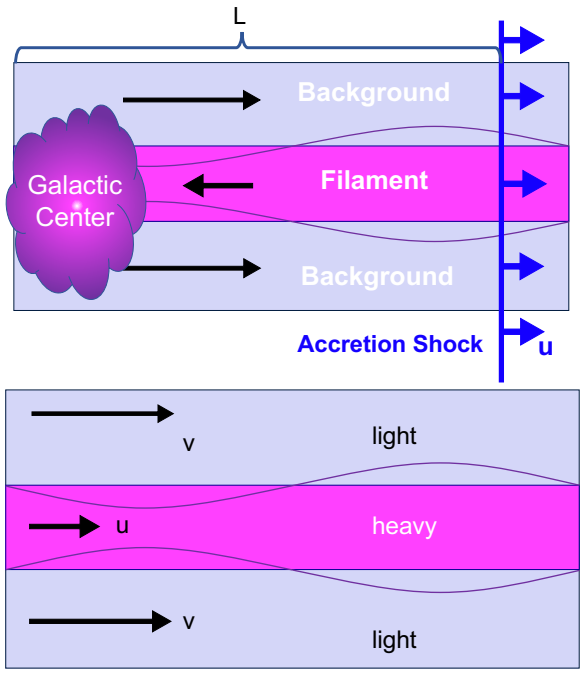

Figure 5.4: Idealized flow geometry of the filament in the laboratory frame (top) and the shock frame (bottom). The velocity gradient present on the filament-gas interface implies that the system is KH unstable. The faint line present in both images is the initial perturbation on the interface.

To determine if the KH instability plays a significant role in the filament's hydrodynamics we compare the KH instability's timescale, $t_{\rm KH}$, to the total time a perturbation can grow before the stream joins the galaxy, $t_{\rm growth}$. The time, $t_{\rm growth}$, is related by the distance between the virial (or accretion) shock and the galactic

center, L, and the velocity of the shock, u. Figure 5.4 shows how L and u relate in an idealized filament. With dimensional analysis, the growth time is given by

$$t_{\text{growth}} \sim \frac{L}{u}. \tag{5.5}$$

Meanwhile, the KH developing on the interface evolves in the linear compressible regime given by growth rate in Equation 5.4 [60]. The corresponding KH timescale is found to be:

$$t_{\text{KH}} \sim \frac{1}{\gamma_{\text{KH}}}. \tag{5.6}$$

While in the linear regime, the amplitude of the perturbation grows as $\exp[t/t_{\text{KH}}]$, indicating that the number of e-foldings, $N_{\text{e-folding}}$ in the perturbation growth is

$$N_{\text{e-folding}} \equiv t_{\text{growth}}/t_{\text{KH}}. \tag{5.7}$$

Mandelkar refers to cases where $N_{\text{e-folding}} \gtrsim 3$ as being quasi-linear and $N_{\text{e-folding}} \gtrsim 10$ as being non-linear [68]. Once the perturbation becomes quasi-linear, the amplitude saturates before it continues to grow in a self similar way [66]. As the growth time increases, the KH instability becomes more disruptive to the filament by mixing the filament and the shocked background. Several turnovers are required during this stage to sufficiently disrupt the filament. Mandelker et. al estimates that the minimum $\text{N}_{\text{e-folding}}$ required to disrupt the stream should exceed three [60, 68]. A scaled, laboratory experiment can determine if the KH growth observed along an idealized filament meets the minimum disruption threshold ($N_{\text{e-folding}} \geq 3$).

5.4 Experimental design

This scaled HED experiment aims to observe KH evolution as it relates to a cosmic filament experiencing a virial shock during galaxy formation. We mimic the idealized version of this process with a cylindrical target designed for the Omega EP laser. Here, a sustained, laser-driven shock travels through a cylindrical shock tube that consists of a plastic rod, or filament, surround by foam, or the background. The shock travels faster in the foam than the rod, and the resulting shear creates a KH-unstable system along the filament interface.

5.4.1 The Physics Package

The cylindrical physics package consists of a 100 μm CHI ($C_{50}H_{47}I_3$) ablator, followed by a narrow (250 μm diameter) plastic rod of density $\rho_{\text{rod}} = 1.4$ g/cm^3 inserted in the center of the low-density foam cylinder of density $\rho_{\text{cyl}} = 140$ mg/cm^3. The plastic rod acts as our filament while the surrounding low-density foam acts as the background. The thermal insulator and the rod are identical in density and material, and contain an iodine dopant (3 atomic %) that is optically thick to the backlighter x-rays.

From here, two different types of targets were developed for this experiment: 'rippled' targets and 'smooth' targets shown on the left and right in Figure 5.5 respectively. In the rippled targets, the filament interface is modulated with a single-mode sine wave of wavelength 200 μm, and a sinusoidal amplitude of $h_0 = 4$ μm (peak-to-valley amplitude $h_{\text{PV}} = 8$ μm) to seed the KH instability along the interface. The amplitude is chosen so that the initial ratio of amplitude to wavelength is very low ($h_0\lambda << 1$) and meets the scaling conditions described in Coffing et. al [60]. The filaments in the smooth targets have no modulations to determine the compression the rod undergoes when the shock passes and subtract it from the instability growth.

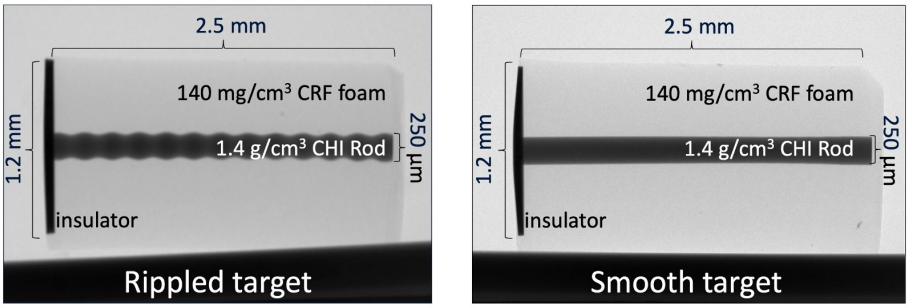

Figure 5.5: X-ray radiographs of an unshocked rippled (left) and smooth (right) target provided by General Atomics. The filament interface on the rippled target is modulated with a single-mode sine wave of wavelength 200 μm, and a peak-to-valley amplitude $h_0 = 8$ μm to seed the KH instability along the interface.

These parameters were chosen so that they fit the astrophysical scaling in [60]. Table 5.1 shows the characteristic parameters that relate the galactic cold stream to the scaled experiment.

5.4.2 Facility Setup

Parameter	Physical Description	Symbol	Cold Stream	Experiment
Length scale [μm]	filament radius	R	3×10^{25}	125
Velocity [μm/ns]	shock speed	u_{shock}	200	20
Density [g/cm^3]	filament density	ρ	10^{-26}	1.4
Ryutov number	hydrodynamic scaling	$\tilde{u}\sqrt{\tilde{\rho}/\tilde{p}}$	2.2	2.3

Table 5.1: Characteristic parameters for the galactic cold stream and scaled experiment. The Ryutov number is discussed in Section 1.4. Adapted from Coffing [60].

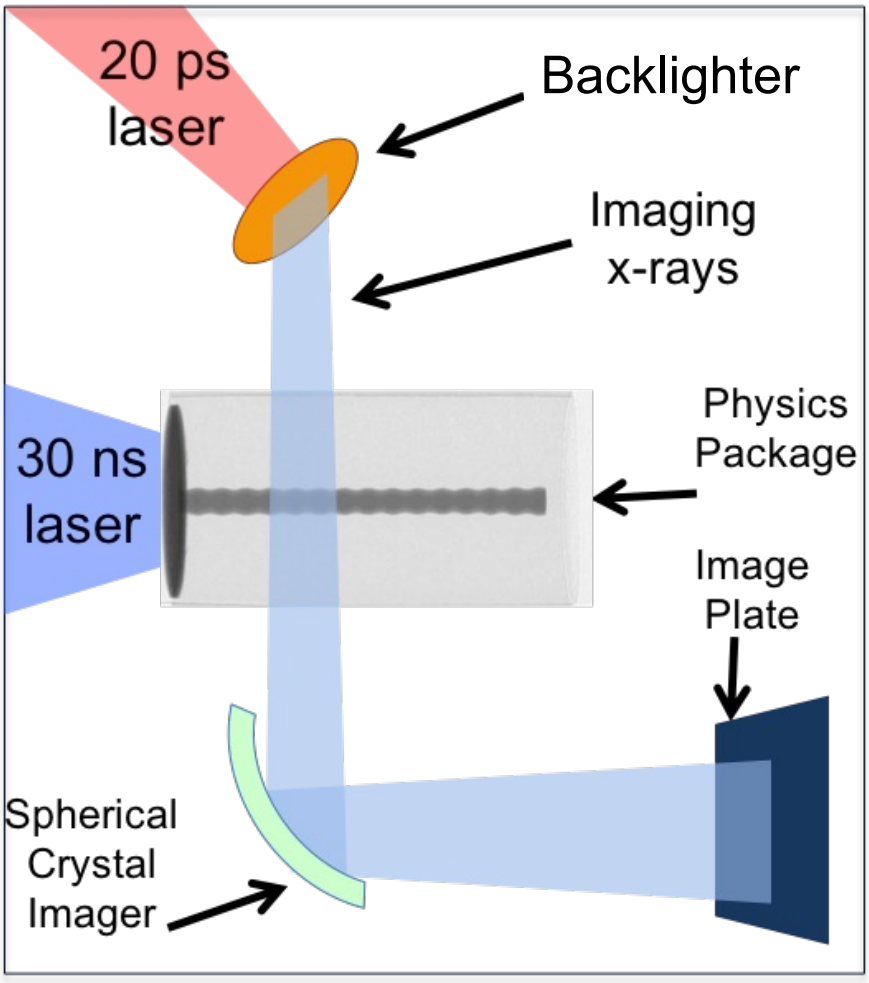

Figure 5.6: A diagram of the experimental setup using the SCI diagnostic for the Cu backlighter with a 20 ps short pulse and image plate detector. The Mn backlighter setup utilizes a 500 ps backlighter pulse and a CCD detector.

Figure 5.6 shows a schematic of the experimental setup using the SCI diagnostic (described in Chapter III) for the Cu backlighter configuration. A $\sim$ 30 ns sustained shock is created by directing 3 subsequent beams with a nominal measured energy of 2200 J/beam for $\sim$ 9 ns, each with a flat spatial profile across the target surface.

Shot Day	Material	X-ray Energy	Laser Pulse	Laser Energy	Detector
HydroDay19	Cu	8.05 keV	20 ps	1500 J	Image Plate
ShockDay20	Mn	6.15 keV	500 ps	250 J	CCD

Table 5.2: This table shows the different backlighter materials and their corresponding properties for the two shot days. The different materials require different laser parameters (pulse lengths and energies) and yield different x-ray energies [30, 36].

Each of the 351 nm beams are smooth with distributed phase plates and has a super-gaussian profile of the form exp[-(r/550 μm)^8], with an expected irradiance of 1.4 $\times 10^{14}$W/ cm^2 where r is the distance from the beams axis.

To diagnose interface evolution, OMEGA EP's fourth beam is focused on the backlighter to create the imaging x-rays. The timing of the fourth beam, simply referred to as 'the timing' here on out, varied shot-to-shot between 60 and 90 ns after the first drive beam to capture the filament dynamics. The timing is listed in the title of the radiographic images shown later in this chapter. The two shot days, HydroDay19 and ShockDay20, described in the next section use different materials for the backlighter and therefore have different pulse requirements. On HydroDay19, the Cu backlighter foil was irradiated with a $\sim$ 1.5 kJ, 20 ps laser pulse to produce the CuK$_\alpha$ photons. For ShockDay20, a long pulse beam is used to create MnHe$_\alpha$ photons by irradiating a thin Mn foil. A 3 ns pre-pulse is used to create an ablation plume of the foil, followed by a 500 ps square pulse [36]. Table 5.2 shows the different backlighter materials and their respective specifications for each shot day.

5.5 Results and Discussion

Two separate shot days were allocated to focus on different aspects of the system. One shot day captured the hydrodynamic and compression behavior of the filament (HydroDay19) and the other determined the shock position (ShockDay20). Each shot day utilized the smooth and rippled target and produced 7 x-ray radiographs. To highlight the different features for each day, targets from the same production batch were imaged using backlighters of differing materials. The CuK$_\alpha$ backlighter emits 8 keV x-rays that are able to image the filament compression and KH features, but are too high energy to produce contrast between the shocked and un-shocked foam. The MnHe$_\alpha$ backlighter emits 6.2 keV x-rays that could successfully discern the shock position, but could not penetrate the higher Z driver. Figure 5.8 shows the

three radiographs that were the primary images used for this analysis due to their contrast, timing, and resolution. The entirety of the radiographs obtained from this campaign are produced in Appendix C.

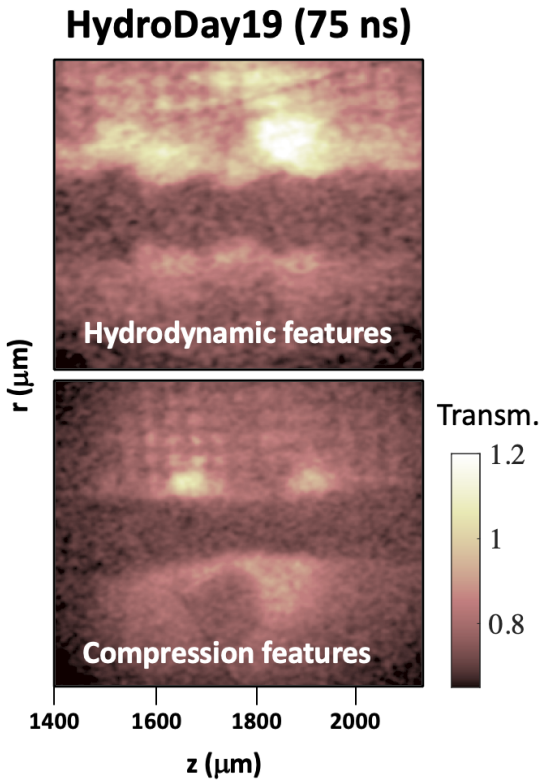

Figure 5.7: Top: An image taken from HydroDay19 of one of the perturbed targets to highlight the hydrodynamic features. Bottom: An image taken from HydroDay19 of one of the smooth targets to highlight the compression features. In both images from HydroDay19, the shock position is indiscernible. The 8 keV backlighter did not provide enough contrast between the shocked and unshocked foam.

We were able to relate the shock positions obtained from ShockDay20 to the hydrodynamics and filament data from HydroDay19 by performing 2-D simulations with the CRASH code. CRASH is an Eulerian, adaptive-mesh-refinement, hydrodynamic code developed at the University of Michigan to simulate experiments in the HED regime [69].

Variations in the laser energy deposition are accounted for with a non-dimensional time-scale. We can obtain a characteristic time-scale for each day by normalizing the

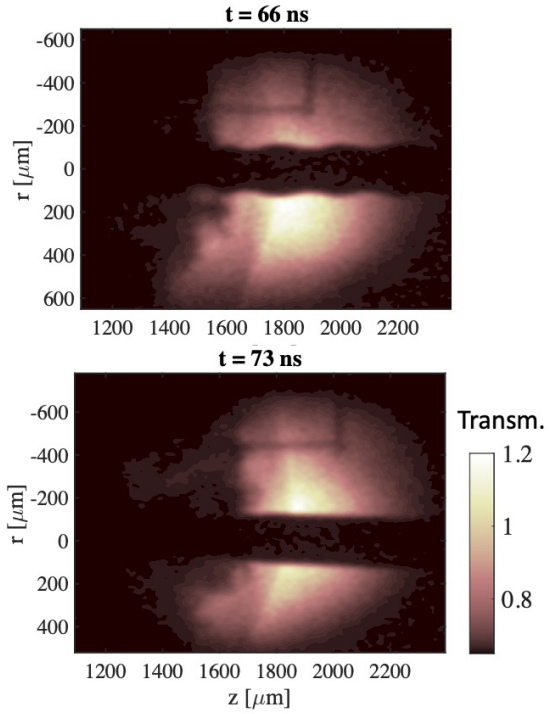

Figure 5.8: Data taken from ShockDay20 at 66 ns (top)and 73 ns (bottom) after the initial laser turns using the Mn backlighter onto a CCD. The shock position is visible but the hydrodynamic features towards the left side of the image are not.

Parameter	Variable	HydroDay19	ShockDay20
Laser Energy [kJ]	E_0	6.6	6.6
Laser Irradiance [TW/cm^2]	I_0	82	66
Target mass [kg]	m	3.2 $\times 10^{-7}$	3.2 $\times 10^{-7}$
Time [ns]	$\tau_{\text{hydro}} = (m/I_0)^{1/3}$	7	7.86

Table 5.3: Hydrodynamic time scales of HydroDay19 and ShockDay20. The parameters are the nominal values requested from the laser facility and target fabrication. The nominal values are relatively consistent between the shot days, and the exact values are given in Appendix C.

energy deposited over well-known initial conditions and experimental parameters. Known and consistent factors between the two experiments are the laser energy, the laser diameter, and the duration of the experiment. The laser energy fluctuates within 8% across the experimental days of interest and the target mass fluctuates within 3%. The exact values obtained in the shown radiographs are given in Appendix C. We use VISRAD to simulate and obtain the projection effect across the target surface to determine the laser irradiance. VISRAD is a 3D view factor code that is used to both design HED physics experiments, and to simulate the multi-dimensional

radiation environment within target systems [70]. The combination of the total mass divided by the laser irradiance raised to the power 1/3 provides the units of second as $\tau_{\text{hydro}} = (m/I_0)^{1/3}$ s.

This produces a characteristic hydrodynamic time scale (τ_{hydro}) for each experimental day [71]. Table 5.3 show the values from each day and their corresponding τ_{hydro}. Finally, dividing the experimental time by their corresponding τ_{hydro} yields a non-dimensional time-scale from which we can plot the shock position. Figure 5.9 shows a plot of the shock position from simulations and the measured shock position from ShockDay20 as a function of the non-dimensional time scale. The plot shows that the simulated shock position from HydroDay19 is in good agreement with the data from ShockDay20. We can now utilize the 2D CRASH simulation to determine the shock position and shock velocity for the relevant images in HydroDay19. The simulated shock velocity at 75 ns for HydroDay19 is 20 μm/ns.

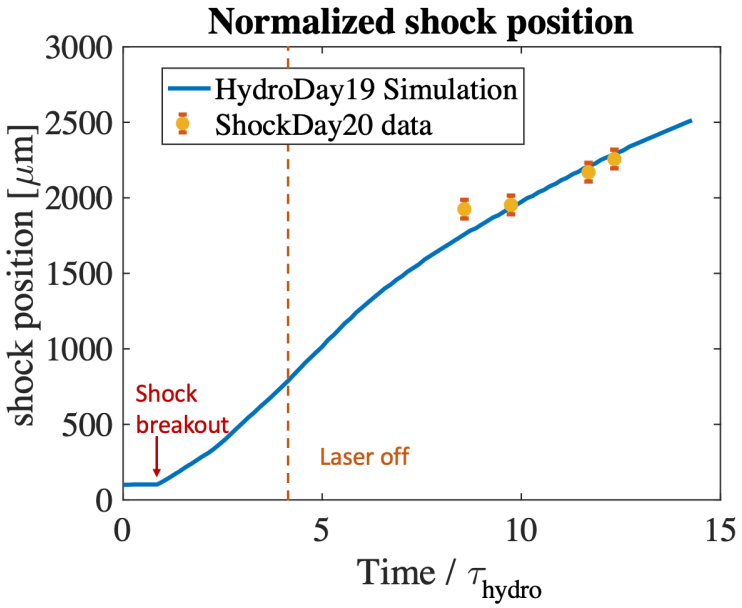

Figure 5.9: The plot compares the simulated shock position to the data from ShockDay20. The shock position is relative to the ablator position and the time is normalized by the hydrodynamic time-scale. The simulated shock appears static until it breaks out into the foam at Time/τ_{hydro} = 0.8, and the laser turns off at Time/τ_{hydro} = 3.8 causing the shock speed to slow down at the times of interest. The data from ShockDay20 is in good agreement with the simulated shock position when normalized by their respective hydrodynamic time-scale τ_{hydro}.

5.5.1 KH growth rate

The KH growth rate is required to determine $N_{e-folding}$ for each peak at 75 ns. To calculate the KH growth rate at 75 ns, we utilize the simulated shock position and velocity for HydroDay19 and relate it to the experimental data. First, the axial distance along the filament is calibrated such that the shock position demarcates the origin and the radiograph is set relative to that position (see Figure 5.10).

The amplitude of each peak is defined as the distance between the peak and the filament interface. We are able to determine the interface location from the planar target on the left in Figure 5.8. The time since the shock has passed each peak is found by dividing the peak's position relative to the shock by the velocity of the shock (nominally 20 μm/ns). We find the time since the shock has passed by dividing these distances by the shock speed. Figure 5.10 shows a plot of the experimentally measured non-dimensional perturbation amplitude h/h_0 vs time since shock passage. The solid points at 10, 19 and 28 ns are the 3 peaks noted in the top image. The dashed line is an exponential fit to the experimental data. Again, the KH amplitude h is expected to grow as $h \sim h_0 e^{\gamma t}$ where γ_{KH} is the KH growth rate and t is the time. Normalizing the y-axis and fitting the exponential of the plot shown in Figure 5.10 yields the instability growth rate of $\gamma_{KH} = .05 \pm .02$ ns^{-1}. The error bounds reflect the fit's 95% confidence level to the plot shown in Figure 5.10.

For this platform and regime, Figure 5.11 shows how $N_{e-folding}$ increases as a function of the position away from the shock. The three peaks present in Figure 5.11 are not in the disruptive regime, but interpolating the line yields that the 6th peak from the shock position crosses the disruption threshold [68, 60]. We find that the experimental filament passes the disruption threshold of $N_{e-folding} > 3$ at ~ 1100 μm away from the shock. Assuming the nominal shock velocity of ~ 20 μm/ns, this corresponds to ~ 55 ns after shock passage; a laser pulse nearly twice as long as that used in this work would be needed to drive this scaled system to full disruption.

5.6 Summary and Future Works

The most proficient star forming galaxies, starburst galaxies, are those that involve filaments that withstand the shock that forms at the edge of the galactic halo and transport matter deep into the galactic disc. The cold, dense matter within the filament moves within the hot gaseous background, indicating that the filament

boundary is likely KH unstable. If the KH instability is allowed enough time to evolve, significant mixing will occur between the hot shocked background and colder dense material and will potentially disrupt the filaments before they can penetrate deeply within the galaxy. Mandelker et. al [68] determines that if $N_{e-folding} \geq 3$ the filament becomes disrupted.

This chapter describes a scaled, HED laboratory experiment on the OMEGA EP laser that emulates and studies the cosmological process of a cold stream penetrating a shocked region. The SCI was used to observe the KH instability on the filament boundary. Analysis of this scaled experiments and tuned simulations revealed that filament disruption due to KH growth begins to occur at distance of ≈ 6 peaks away from the shock. This information can inform large-scale astrophysical simulations, unable to resolve small-scale hydrodynamic instabilities, on when mass delivery to the galactic disc may be inhibited.

Future works would benefit from studying the dependency between mixing- and instability related quantities such as the wavelength and Atwood number. Performing this experiment on a more energetic laser facility would allow us to incorporate the effects from radiative cooling. Additionally, conducting experiments in a rectilinear coordinate system would provide a higher contrast along the filament interface.

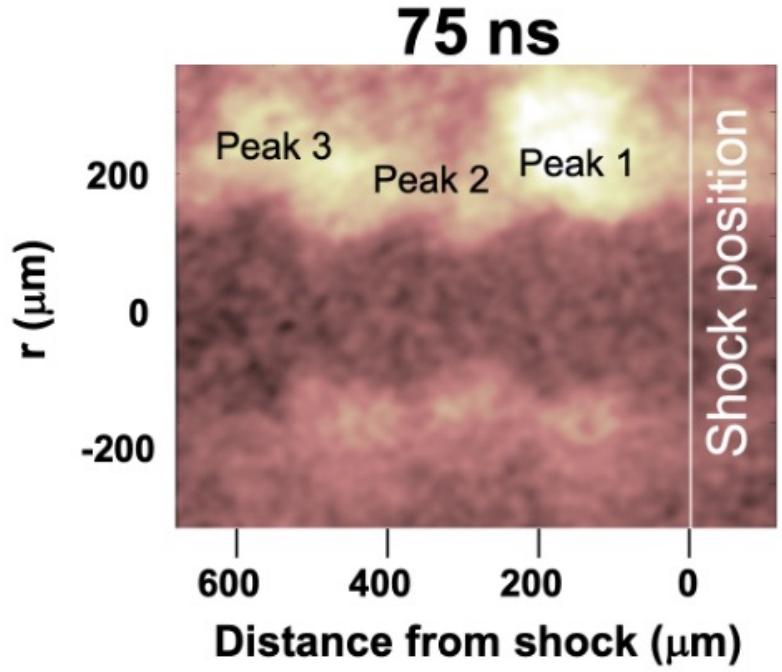

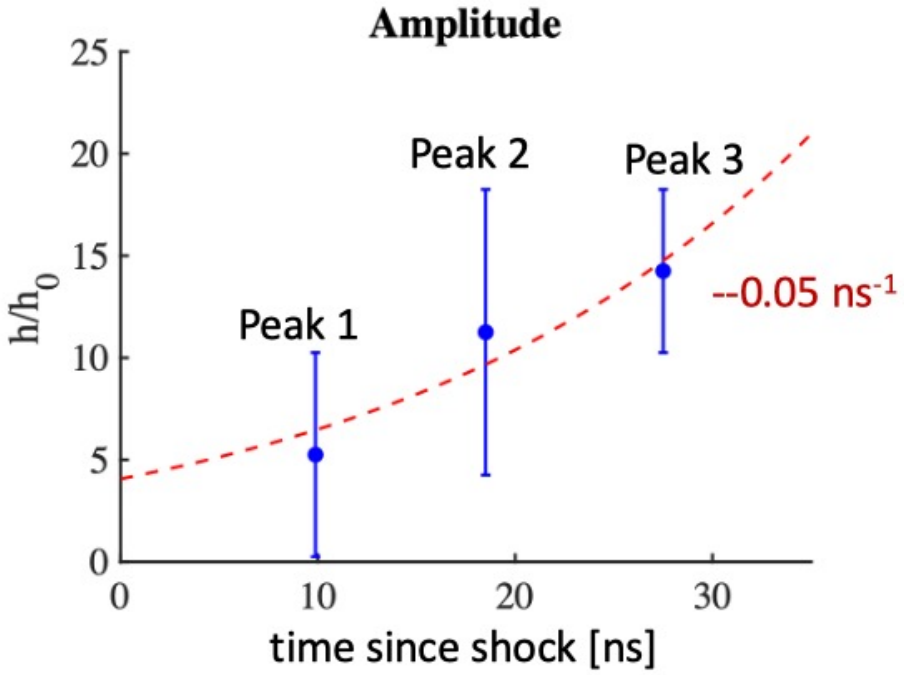

Figure 5.10: (Top) Experimental radiograph taken at 75 ns from HydroDay19 showing three distinct perturbations at different times in their evolution. (Bottom) The average amplitude (height) of each peak extracted from the data in Figure 5.8. The height is determined from the planar interface to the tip. The error is calculated using the 5% - 95% edge measurement. The time since the shock has passed shown in the x-axis is obtained from the validated simulations. The fit of the three peaks yields is shown by the dashed red line and represents the linear KH instability growth rate, $\gamma_{\mathrm{KH}} = .05 \pm .02$ ns^{-1}.

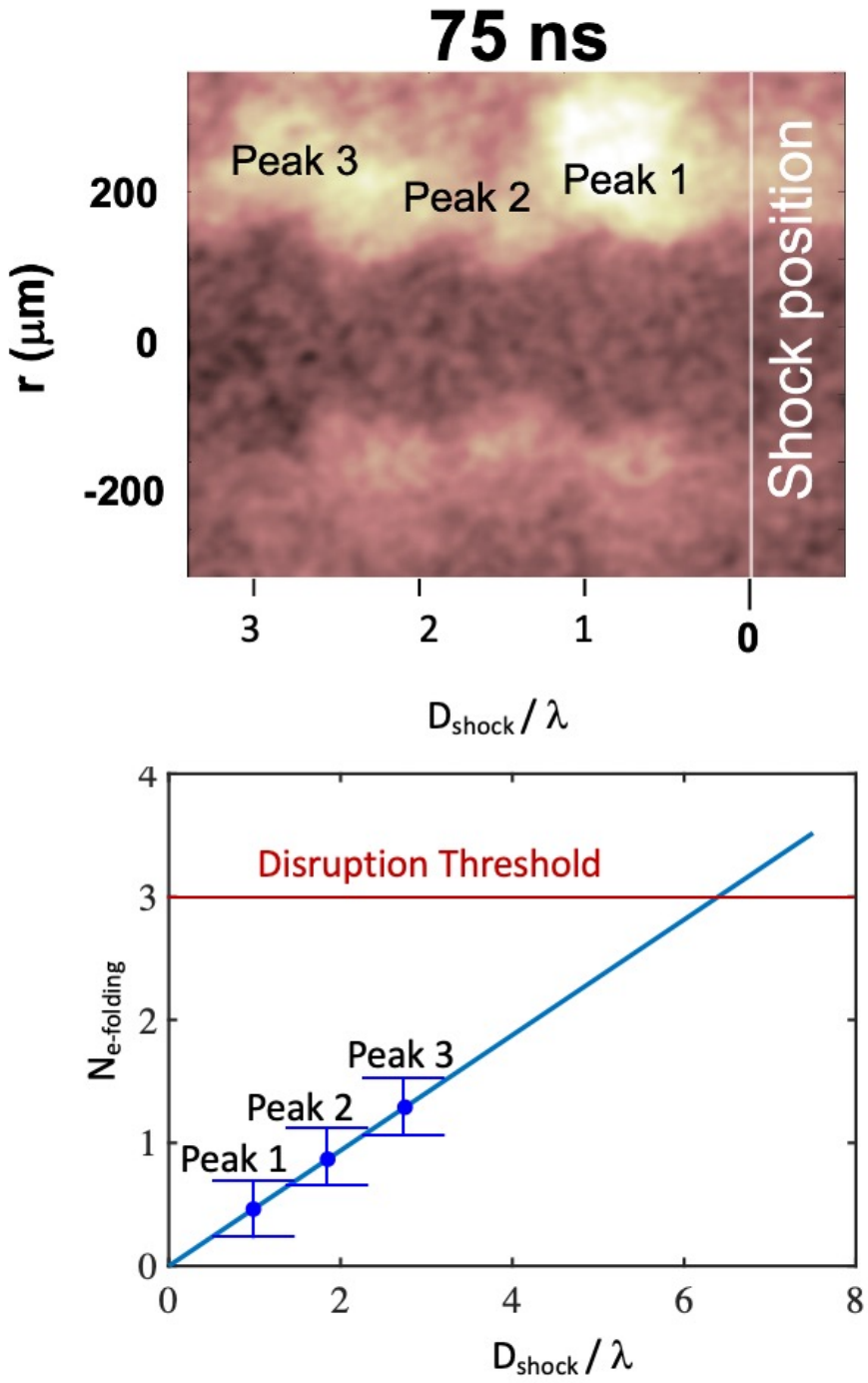

Figure 5.11: (Top) X-ray radiograph at t = 75 ns from HydroDay19 with the simulated shock position imposed over the image. The x-axis is set relative to shock position and is normalized over the perturbation wavelength (200 μm). (Bottom) $N_{e-folding}$ for each peak labeled in the top figure as a function of the distance from the normalized shock position. The error is propagated from γ_{KH}. The disruption threshold is said to occur when $N_{e-folding} \sim 3$ and is noted as the horizontal solid red line in the figure. The three peaks present in the data from HydroDay19 are not in the disruptive regime, but interpolating the line yields that the 6th peak from the shock position crosses the disruption threshold [60, 68].

CHAPTER VI

Summary and Conclusion

In this thesis, I presented two original works of research: one as an experimental lead on the OMEGA EP laser, and one as a campaign designer on the NIF. While different, both projects investigate the effects of a specific type of hydrodynamic instability in the shock-drive, HED regime.

In Chapter II, I discuss the governing equations of fluid dynamics that we use to describe certain HED systems. Because these systems are described as a fluid, they are also subjected to hydrodynamic instabilities. These instabilities are observable on a vast range of length scales from supernova-remnants to inertial confinement fusion capsules. The Kelvin-Helmholtz instability develops at the interface between two horizontal parallel fluid streams with different velocities and densities. To determine the KH instability growth rate, the conditions are first simplified and linearized. Ultimately, the instability growth rate is dependent on the wavenumber, velocity difference between the surface, and the density ratio of the fluids. The Rayleigh-Taylor instability develops when pressure gradient is misaligned with the density gradient. The RT growth rate is dependent on the interface acceleration, wavenumber, and density ratio. Both the RT and the KH instabilities begin to develop vorticies as they enter the nonlinear regime. Vorticity is deposited on an interface when a shock wave interacts with the material interface at a non-normal angle and can lead to a transition to turbulence. Turbulence has been studied quite prolifically for more than a century and has a multitude of definitions across a wide range of subfields in physics.

In Chapter III, I introduced a common method to observe hydrodynamic instabilities in HED experiments with x-ray diagnostics. I described the mechanics behind the Crystal Backlighter Imager and Spherical Crystal Imager, both spherically bent

crystals located at the National Ignition Facility and Laser for Laboratory Energetics respectively.

In Chapter IV, I described a campaign conducted on the National Ignition Facility that sought to improve experimental resolution by changing key parameters in the x-ray diagnostic and the target. I described a series of radiation hydrodynamic simulations I performed using the LLNL code, HYDRA to inform target and diagnostic designs for multiple shot days. I then showed the resulting experimental radiographs taken on the NIF that resolve the fine-scale features expected in these RT unstable systems with unprecedented clarity.

However, even with these improvements, the necessary spatial scales were not resolvable. Pre-shot and post-shot HYDRA simulations highlighted the importance of reducing the motion blur. To do so, the initial foam density increased from 85 mg/cm^3 in the VoRTex campaign to 145 mg/cm^3 in the HRT campaign to slow down the mixing dynamics, while the backlighter resolution was reduced from 600 ps to 100 ps. Spectral analysis of the rollup and shocked foam in the radiograph from shot N200809 shows different magnitudes in the two regions. This indicates that there are discernible fluctuations between the two regions. However, neither region exhibit the $k^{-5/3}$ spectrum decay that would identify the existence of the inertial subrange. However, post-shot simulations do indicate that the rollup region achieves the minimum-state Reynolds number criteria indicating that the region is possibly turbulent.

Future experiments interested in directly measuring the Liepmann-Taylor scales in an HED platform would benefit from a variety of alterations. For one, looking at a different region with a larger characteristic length scale would create larger, and possibly resolvable, Liepmann-Taylor scales. A system with a larger energy-injection length scale L such as a KH-unstable platform, would yield a larger Liepmann-Taylor scale that might be detectable by the resolution capabilities of current diagnostics.

In Chapter V, I describe a scaled, HED laboratory experiment on the OMEGA EP laser that emulates and studies the cosmological process of a cold stream penetrating a shocked region. The SCI was used to observe the KH instability on the filament boundary. To account for variations in the laser energy deposition and simulations, I scale the two radiographs to the same, non-dimensional time scale. Once I am able to

relate the simulated shock position to the data, I determine the KH growth rate for HydroDay19 is $\gamma_{\mathrm{KH}} = .05 \pm .02$ ns^{-1}. Finally, I determine that the three peaks visible in the data do not disrupt the filament. However, the line interpolation indicates that filament disruption due to KH growth occurs at distance of ≈ 6 peaks away from the shock. This information can inform large-scale astrophysical simulations, unable to resolve small-scale hydrodynamic instabilities, on when mass delivery to the galactic disc may be inhibited.

Future works would benefit from studying the dependency between mixing- and instability related quantities such as the wavelength and Atwood number. Performing this experiment on a more energetic laser facility would allow us to incorporate the effects from radiative cooling. Additionally, conducting experiments in a rectilinear coordinate system would provide a higher contrast along the filament interface.

APPENDICES

APPENDIX A

Supporting data for the HRT campaign

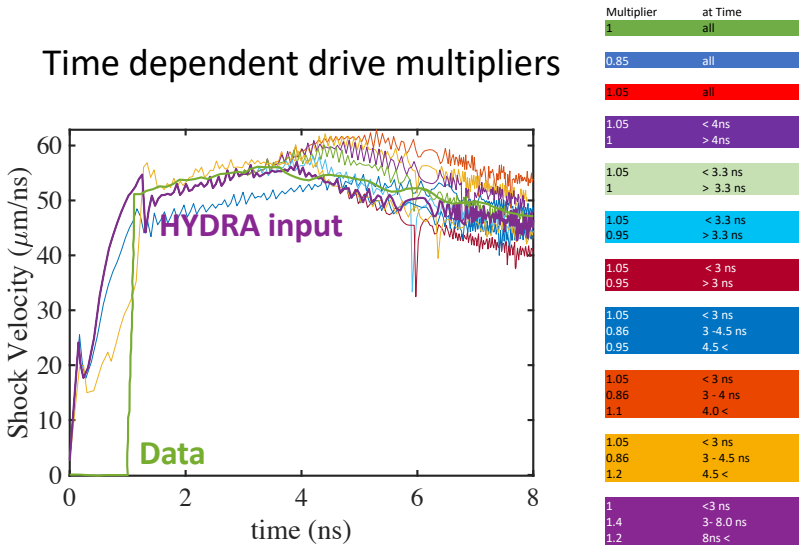

Figure A.1: Time dependent drive multipliers used for the HYDRA simulations.

BIBLIOGRAPHY

BIBLIOGRAPHY

[1] Yuval Birnboim and Avishai Dekel. Virial shocks in galactic haloes? *Monthly Notices of the Royal Astronomical Society*, 345(1):349–364, 10 2003.

[2] A. Dekel, Y. Birnboim, G. Engel, J. Freundlich, T. Goerdt, M. Mumcuoglu, E. Neistein, C. Pichon, R. Teyssier, and E. Zinger. Cold streams in early massive hot haloes as the main mode of galaxy formation. *Nature*, 457(7228):451–454, January 2009.

[3] J. S. Dunlop, R. J. McLure, A. D. Biggs, J. E. Geach, M. J. Michałowski, R. J. Ivison, W. Rujopakarn, E. van Kampen, A. Kirkpatrick, A. Pope, D. Scott, A. M. Swinbank, T. A. Targett, I. Aretxaga, J. E. Austermann, P. N. Best, V. A. Bruce, E. L. Chapin, S. Charlot, M. Cirasuolo, K. Coppin, R. S. Ellis, S. L. Finkelstein, C. C. Hayward, D. H. Hughes, E. Ibar, P. Jagannathan, S. Khochfar, M. P. Koprowski, D. Narayanan, K. Nyland, C. Papovich, J. A. Peacock, G. H. Rieke, B. Robertson, T. Vernstrom, P. P. van der Werf, G. W. Wilson, and M. Yun. A deep ALMA image of the Hubble Ultra Deep Field. *Monthly Notices of the Royal Astronomical Society*, 466(1):861–883, 11 2016.

[4] Jonathan P. Gardner, John C. Mather, Mark Clampin, Rene Doyon, Kathryn A. Flanagan, Marijn Franx, Matthew A. Greenhouse, Heidi B. Hammel, John B. Hutchings, Peter Jakobsen, Simon J. Lilly, Jonathan I. Lunine, Mark J. McCaughrean, Matt Mountain, George H. Rieke, Marcia J. Rieke, George Sonneborn, Massimo Stiavelli, Rogier Windhorst, and Gillian S. Wright. The james webb space telescope. In Harley A. Thronson, Massimo Stiavelli, and Alexander Tielens, editors, *Astrophysics in the Next Decade*, pages 1–29, Dordrecht, 2009. Springer Netherlands.

[5] R Paul Drake, Eric C Harding, and Carolyn C Kuranz. Approaches to turbulence in high-energy-density experiments. *Physica Scripta*, T132:014022, dec 2008.

[6] R. P. Drake. Perspectives on high-energy-density physics. *Physics of Plasmas*, 16(5):055501, 2009.

[7] R. Paul Drake. *High-energy-density physics foundation of inertial fusion and experimental astrophysics*. Springer, 2019.

[8] B.L. Henke, E.M. Gullikson, and J.C. Davis. X-ray interactions: photoabsorption, scattering, transmission, and reflection at e=50-30000 ev, z=1-92. *tomic Data and Nuclear Data Tables*, 54(2):181–342, 1993.

[9] John Nuckolls, Lowell Wood, Albert Thiessen, and George. Laser compression of matter to super-high densities: Thermonuclear (ctr) applications. *Nature*, 239:139–142, 09 1972.

[10] D. D. Ryutov. Scaling laws for dynamical plasma phenomena. *Physics of Plasmas*, 25(10):100501, 2018.

[11] R Paul Drake. *High-Energy-Density Physics*. Springer International Publishing, 2018.

[12] Bruce A. Remington, R. Paul Drake, and Dmitri D. Ryutov. Experimental astrophysics with high power lasers and z pinches. *Rev. Mod. Phys.*, 78:755–807, Aug 2006.

[13] R. E. Marshak. Effect of radiation on shock wave behavior. *The Physics of Fluids*, 1(1):24–29, 1958.

[14] Jeffrey P. Freidberg. *Plasma Physics and Fusion Energy*. Cambridge University Press, 2007.

[15] Rayleigh and John William Strutt. Investigation of the Character of the Equilibrium of an Incompressible Heavy Fluid of Variable Density, December 2011.

[16] Geoffrey Ingram Taylor. The instability of liquid surfaces when accelerated in a direction perpendicular to their planes. i. *Proceedings of the Royal Society of London. Series A. Mathematical and Physical Sciences*, 201(1065):192–196, 1950.

[17] A. M. Rasmus, C. A. Di Stefano, K. A. Flippo, F. W. Doss, J. L. Kline, J. D. Hager, E. C. Merritt, T. R. Desjardins, W. C. Wan, T. Cardenas, D. W. Schmidt, P. M. Donovan, F. Fierro, J. I. Martinez, J. S. Zingale, and C. C. Kuranz. Shock-driven discrete vortex evolution on a high-atwood number oblique interface. *Physics of Plasmas*, 25(3):032119, 2018.

[18] Ye Zhou. Rayleigh–taylor and richtmyer–meshkov instability induced flow, turbulence, and mixing. ii. *Physics Reports*, 723-725:1 – 160, 2017. Rayleigh–Taylor and Richtmyer–Meshkov instability induced flow, turbulence, and mixing. II.

[19] Ye Zhou. Unification and extension of the similarity scaling criteria and mixing transition for studying astrophysics using high energy density laboratory experiments or numerical simulations. *Physics of Plasmas*, 14(8):082701, 2007.

[20] Jeffrey W Jacobs and JM Sheeley. Experimental study of incompressible richtmyer–meshkov instability. *Physics of Fluids*, 8(2):405–415, 1996.

[21] Ye Zhou, Timothy T Clark, Daniel S Clark, S Gail Glendinning, M Aaron Skinner, Channing M Huntington, Omar A Hurricane, Andris M Dimits, and Bruce A Remington. Turbulent mixing and transition criteria of flows induced by hydrodynamic instabilities. *Physics of Plasmas*, 26(8):080901, 2019.

[22] HF Robey, Ye Zhou, AC Buckingham, P Keiter, BA Remington, and RP Drake. The onset of turbulence in high reynolds number, accelerated flows. part ii. experiment. *Physics of Plasmas*, 10, 2003.

[23] Paul E Dimotakis. The mixing transition in turbulent flows. *Journal of Fluid Mechanics*, 409:69–98, 2000.

[24] Guy Dimonte and Robert Tipton. K-l turbulence model for the self-similar growth of the rayleigh-taylor and richtmyer-meshkov instabilities. *Physics of Fluids*, 18(8):085101, 2006.

[25] H. Tennekes and J.L. Lumley. *A FIRST COURSE IN TURBULENCE*. MIT PRESS, 1978.

[26] Katepalli R. Sreenivasan. On the universality of the kolmogorov constant. *Physics of Fluids*, 7(11):2778–2784, 1995.

[27] Jiro Shimoda, Takuya Akahori, A Lazarian, Tsuyoshi Inoue, and Yutaka Fujita. Discovery of Kolmogorov-like magnetic energy spectrum in Tycho's supernova remnant by two-point correlations of synchrotron intensity. *Monthly Notices of the Royal Astronomical Society*, 480(2):2200–2205, 07 2018.

[28] KA Flippo, JL Kline, FW Doss, EN Loomis, M Emerich, B Devolder, TJ Murphy, KB Fournier, DH Kalantar, SP Regan, et al. Development of a big area backlighter for high energy density experiments. *Review of Scientific Instruments*, 85(9):093501, 2014.

[29] S. R. Nagel, K.S. Raman, C. M. Huntington, S. A. MacLaren, P. Wang, M. A. Barrios, T. Baumann, J. D. Bender, L. R. Benedetti, D. M. Doane, S. Felker, P. Fitzimmons, K. A. Flippo, J. P. Holder, Kaczala. D. N., T. S. Perry, R. M. Seugling, L. Savage, and Y. Zhou. A platform for studying the rayleigh-taylor and richtmyer-meshkov instabilities in a planar geometry at high energy density at the national ignition facility. *Physics of Plasmas*, 913:103–106, 2019.

[30] G. N. Hall, C. M. Krauland, M. S. Schollmeier, G. E. Kemp, J. G. Buscho, R. Hibbard, N. Thompson, E. R. Casco, M. J. Ayers, S. L. Ayers, N. B. Meezan, L. F. Berzak Hopkins, R. Nora, B. A. Hammel, L. Masse, J. E. Field, D. K. Bradley, P. Bell, O. L. Landen, J. D. Kilkenny, D. Mariscal, J. Park, T. J. McCarville, R. Lowe-Webb, D. Kalantar, T. Kohut, and K. Piston. The crystal backlighter imager: A spherically bent crystal imager for radiography on the national ignition facility. *Review of Scientific Instruments*, 90(1):013702, 2019.

[31] C. Stoeckl, G. Fiksel, D. Guy, C. Mileham, P. M. Nilson, T. C. Sangster, M. J. Shoup, and W. Theobald. A spherical crystal imager for OMEGA EP. *Review of Scientific Instruments*, 83(3):033107, March 2012.

[32] W. L. Bragg. The diffraction of short electromagnetic waves by a crystal. *Scientia*, 23(45):153, 1929.

[33] Marius S. Schollmeier, Matthias Geissel, Jonathon E. Shores, Ian C. Smith, and John L. Porter. Performance of bent-crystal x-ray microscopes for high energy density physics research. *Appl. Opt.*, 54(16):5147–5161, Jun 2015.

[34] Marius Schollmeier and Guillaume Loisel. Systematic search for spherical crystal x-ray microscopes matching 1–25 kev spectral line sources. *The Review of scientific instruments*, 87:123511, 12 2016.

[35] Donna Strickland and Gerard Mourou. Compression of amplified chirped optical pulses. *Optics Communications*, 56(3):219–221, 1985.

[36] C. Fiedler Kawaguchi, K. A. Flippo, A. M. Rasmus, B. Tobias, T. Byvank, C. A. Di Stefano, E. C. Merritt, F. W. Doss, K. V. Kelso, N. N. Vazirani, C. Stoeckl, M. Bedzyk, R. Jungquist, and C. Mileham. Improved imaging using mn he- x rays at omega ep. *Review of Scientific Instruments*, 92(9):093508, 2021.

[37] A. Do, A. M. Angulo, S. R. Nagel, G. N. Hall, D. K. Bradley, W. W. Hsing, L. A. Pickworth, N. Izumi, H. F. Robey, and Y. Zhou. High spatial resolution and contrast radiography of hydrodynamic instabilities at the national ignition facility. *Physics of Plasmas*, 29(8):080703, 2022.

[38] A. Do, A. M. Angulo, G. N. Hall, S. R. Nagel, N. Izumi, B. J. Kozioziemski, T. McCarville, J. M. Ayers, and D. K. Bradley. X-ray imaging of rayleigh taylor instabilities using fresnel zone plate at the national ignition facility. *Review of Scientific Instruments*, 92(5):053511, 2021.

[39] S. Glenn, J. Koch, D. K. Bradley, N. Izumi, P. Bell, J. Holder, G. Stone, R. Prasad, A. MacKinnon, P. Springer, O. L. Landen, and G. Kyrala. A hardened gated x-ray imaging diagnostic for inertial confinement fusion experiments at the national ignition facility. *Review of Scientific Instruments*, 81(10):10E539, 2010.

[40] A.M. Angulo, S. Nagel, Channing Huntington, C. Weber, Harry Robey, G.N. Hall, L. Pickworth, and C. Kuranz. Design of a high-resolution rayleigh-taylor experiment with the crystal backlighter imager on the national ignition facility. *Journal of Instrumentation*, 17:P02025, 02 2022.

[41] H. F. Robey, Ye Zhou, A. C. Buckingham, P. Keiter, B. A. Remington, and R. P. Drake. The time scale for the transition to turbulence in a high reynolds number, accelerated flow. *Physics of Plasmas*, 10(3):614–622, 2003.

[42] Vladimir Smalyuk, Harry Robey, D.T. Casey, D. Clark, T. Döppner, S. Haan, B.A. Hammel, Andrew Macphee, David Martinez, Jose Milovich, Luc Peterson, L. Pickworth, Jesse Pino, Kisha Raman, R. Tipton, C.R. Weber, K.L. Baker, Benjamin Bachmann, L.F. Hopkins, and M. Johnson. Mix and hydrodynamic instabilities on nif. *Journal of Instrumentation*, 12:C06001–C06001, 06 2017.

[43] O A Hurricane. Overview of progress and future prospects in indirect drive implosions on the national ignition facility. *Journal of Physics: Conference Series*, 717:012005, may 2016.

[44] D. Clark, C. Weber, Jose Milovich, A. Pak, D. Casey, B. Hammel, D. Ho, O. Jones, Joseph Koning, Andrea Kritcher, M. Marinak, L. Masse, David Munro, Mehul Patel, Premsai Patel, Harry Robey, C. Schroeder, S. Sepke, and M. Edwards. Three-dimensional modeling and hydrodynamic scaling of national ignition facility implosions. *Physics of Plasmas*, 26:050601, 05 2019.

[45] Rebecca M Darlington, Thomas L McAbee, and Garry Rodrigue. A study of ale simulations of rayleigh–taylor instability. *Computer Physics Communications*, 135(1):58–73, 2001.

[46] AR Miles. Bubble merger model for the nonlinear rayleigh–taylor instability driven by a strong blast wave. *Physics of plasmas*, 11(11):5140–5155, 2004.

[47] H. F. Robey, Ye Zhou, A. C. Buckingham, P. Keiter, B. A. Remington, and R. P. Drake. The time scale for the transition to turbulence in a high reynolds number, accelerated flow. *Physics of Plasmas*, 10(3):614–622, 2003.

[48] Lord Rayleigh. Scientific papers ii, 200. *Cambridge, England*, 1900.

[49] Geoffrey Ingram Taylor. The instability of liquid surfaces when accelerated in a direction perpendicular to their planes. i. *Proceedings of the Royal Society of London. Series A. Mathematical and Physical Sciences*, 201(1065):192–196, 1950.

[50] MS Roberts and Jeffrey W Jacobs. The effects of forced small-wavelength, finite-bandwidth initial perturbations and miscibility on the turbulent rayleigh–taylor instability. *Journal of Fluid Mechanics*, 787:50–83, 2016.

[51] Ye Zhou, BA Remington, HF Robey, AW Cook, SG Glendinning, A Dimits, AC Buckingham, GB Zimmerman, EW Burke, TA Peyser, et al. Progress in understanding turbulent mixing induced by rayleigh–taylor and richtmyer–meshkov instabilities. *Physics of Plasmas*, 10(5):1883–1896, 2003.

[52] Steven H. Langer, Ian Karlin, and Michael M. Marinak. Performance characteristics of hydra –a multi-physics simulation code from llnl. In Michel Daydé, Osni Marques, and Kengo Nakajima, editors, *High Performance Computing for Computational Science – VECPAR 2014*, pages 173–181, Cham, 2015. Springer International Publishing.

[53] M. M. Marinak, G. D. Kerbel, N. A. Gentile, O. Jones, D. Munro, S. Pollaine, T. R. Dittrich, and S. W. Haan. Three-dimensional hydra simulations of national ignition facility targets. *Physics of Plasmas*, 8(5):2275–2280, 2001.

[54] R M Malone, J R Bower, D K Bradley, G A Capelle, J R Celeste, P M Celliers, G W Collins, M J Eckart, J H Eggert, B C Frogget, R L Guyton, D G Hicks, M I Kaufman, B J MacGowan, S Montelongo, E W Ng, R B Robinson, T W Tunnell, P W Watts, and P G Zapata. Imaging visar diagnostic for the national ignition facility (nif).

[55] E. L. Dewald, K. M. Campbell, R. E. Turner, J. P. Holder, O. L. Landen, S. H. Glenzer, R. L. Kauffman, L. J. Suter, M. Landon, M. Rhodes, and D. Lee. Dante soft x-ray power diagnostic for national ignition facility. *Review of Scientific Instruments*, 75(10):3759–3761, 2004.

[56] S. Glenn, J. Koch, D. K. Bradley, N. Izumi, P. Bell, J. Holder, G. Stone, R. Prasad, A. MacKinnon, P. Springer, O. L. Landen, and G. Kyrala. A hardened gated x-ray imaging diagnostic for inertial confinement fusion experiments at the national ignition facility. *Review of Scientific Instruments*, 81(10):10E539, 2010.

[57] P. Tzeferacos, A. Rigby, A. F. Bott, A. R. Bell, R. Bingham, A. Casner, F. Cattaneo, E. M. Churazov, J. Emig, F. Fiuza, and et al. Laboratory evidence of dynamo amplification of magnetic fields in a turbulent plasma. *Nature Communications*, 9(1), 2018.

[58] G. Rigon, B. Albertazzi, T. Pikuz, P. Mabey, V. Bouffetier, N. Ozaki, T. Vinci, F. Barbato, E. Falize, Y. Inubushi, and et al. Micron-scale phenomena observed in a turbulent laser-produced plasma. *Nature Communications*, 12(1), 2021.

[59] Cris Barnes, N. Elliott, s Batha, N. Lanier, G. Magelssen, John Scott, Steve Rothman, Colin Horsfield, A. Dunne, and K. Parker. Characterization of surface roughness and initial conditions for cylindrical hydrodynamic and mix experiments. *Fusion Science and Technology*, 41, 05 2002.

[60] Shane X. Coffing, Adriana A. Angulo, Matthew R. Trantham, Yuval Birnboim, Carolyn C. Kuranz, R. P. Drake, and Guy Malamud. Design and scaling of an omega-EP experiment to study cold streams feeding early galaxies. *The Astrophysical Journal Supplement Series*, 245(2):27, dec 2019.

[61] Volker Springel, Simon D M White, Adrian Jenkins, Carlos S Frenk, Naoki Yoshida, Liang Gao, Julio Navarro, Robert Thacker, Darren Croton, John Helly, John A Peacock, Shaun Cole, Peter Thomas, Hugh Couchman, August Evrard, Jörg Colberg, and Frazer Pearce. Simulating the joint evolution of quasars, galaxies and their large-scale distribution. *Nature*, 435:629–636, 2005.

[62] M. J. Rees and J. P. Ostriker. Cooling, dynamics and fragmentation of massive gas clouds: clues to the masses and radii of galaxies and clusters. *Monthly Notices of the Royal Astronomical Society*, 179(4):541–559, 08 1977.

[63] S. D. M. White and M. J. Rees. Core condensation in heavy halos: a two-stage theory for galaxy formation and clustering. *Monthly Notices of the Royal Astronomical Society*, 183(3):341–358, 07 1978.

[64] Francesco Haardt and Piero Madau. Radiative transfer in a clumpy universe. iv. new synthesis models of the cosmic uv/x-ray background. *The Astrophysical Journal*, 746(2):125, feb 2012.

[65] Andrew J. Benson and Richard Bower. Accretion shocks and cold filaments in galaxy formation. *Monthly Notices of the Royal Astronomical Society*, 410(4):2653–2661, 01 2011.

[66] Nir Mandelker, Dan Padnos, Avishai Dekel, Yuval Birnboim, Andreas Burkert, Mark R. Krumholz, and Elad Steinberg. Instability of supersonic cold streams feeding galaxies – I. Linear Kelvin–Helmholtz instability with body modes. *Monthly Notices of the Royal Astronomical Society*, 463(4):3921–3947, 09 2016.

[67] G. Malamud, A. Shimony, W.C. Wan, C.A. Di Stefano, Y. Elbaz, C.C. Kuranz, P.A. Keiter, R.P. Drake, and D. Shvarts. A design of a two-dimensional, supersonic kh experiment on omega-ep. *High Energy Density Physics*, 9(4):672–686, 2013.

[68] Nir Mandelker, Daisuke Nagai, Han Aung, Avishai Dekel, Yuval Birnboim, and Frank C van den Bosch. Instability of supersonic cold streams feeding galaxies – IV. Survival of radiatively cooling streams. *Monthly Notices of the Royal Astronomical Society*, 494(2):2641–2663, 04 2020.

[69] B. van der Holst, G. Tóth, I. V. Sokolov, K. G. Powell, J. P. Holloway, E. S. Myra, Q. Stout, M. L. Adams, J. E. Morel, S. Karni, B. Fryxell, and R. P. Drake. Crash: A block-adaptive-mesh code for radiative shock hydrodynamics—implementation and verification. *The Astrophysical Journal Supplement Series*, 194(2):23, may 2011.

[70] J.J. MacFarlane. Visrad—a 3-d view factor code and design tool for high-energy density physics experiments. *Journal of Quantitative Spectroscopy and Radiative Transfer*, 81(1):287–300, 2003. Radiative Properties of Hot Dense Matter.

[71] N. C. Swisher, C. C. Kuranz, D. Arnett, O. Hurricane, B. A. Remington, H. F. Robey, and S. I. Abarzhi. Rayleigh-taylor mixing in supernova experiments. *Physics of Plasmas*, 22(10):102707, 2015.